The high charge fraction of flame-generated particles in the size range below 3 nm measured by enhanced particle detectors

Wang, Yang

2017-02

Wang , Y , Kangasluoma , J , Attoui , M , Fang , J , Junninen , H , Kulmala , M , Petäjä , T & Biswas , P 2017 , ' The high charge fraction of flame-generated particles in the size range below 3 nm measured by enhanced particle detectors ' , Combustion and Flame , vol. 176 , pp. 72-80 . https://doi.org/10.1016/j.combustflame.2016.10.003

http://hdl.handle.net/10138/307935
https://doi.org/10.1016/j.combustflame.2016.10.003

Elsevier Editorial System(tm) for Combustion and Flame

Manuscript Draft

Manuscript Number: CNF-D-16-00346R3

Title: The High Charge Fraction of Flame-generated Particles in the Size Range below 3 nm Measured by Enhanced Particle Detectors

Article Type: Accepted Paper

Keywords: flame synthesis; charge fraction; sub-3 nm particle; titanium dioxide; differential mobility analyzer; mass spectrometry

Corresponding Author: Prof. Pratim Biswas, Ph. D.

Corresponding Author's Institution: Washington University in St. Louis

First Author: Yang Wang, B.S.

Order of Authors: Yang Wang, B.S.; Juha Kangasluoma, Ph.D.; Michel Attoui, Ph.D.; Jiaxi Fang, Ph.D.; Heikki Junninen, Ph.D.; Markku Kulmala, Ph.D.; Tuukka Petäjä, Ph.D.; Pratim Biswas, Ph. D.

Manuscript Region of Origin: USA

The High Charge Fraction of Flame-generated Particles in the Size Range below 3 nm Measured by Enhanced Particle Detectors

Yang Wang[1], Juha Kangasluoma[2], Michel Attoui[2,3], Jiaxi Fang[1], Heikki Junninen[2], Markku Kulmala[2], Tuukka Petäjä[2], and Pratim Biswas[1*]

[1] Aerosol and Air Quality Research Laboratory
Department of Energy, Environmental & Chemical Engineering
Washington University in St. Louis
St. Louis, Missouri 63130, USA

[2] Department of Physics,
University of Helsinki, P.O. Box 64, Helsinki, 00014, Finland

[3] LISA Université Paris Est, Diderot, Créteil, 7583, France

2nd Revised Version Submitted: September 30, 2016

Original Submitted to:
Combustion and Flame
May 30, 2016

* To whom correspondence should be addressed:

Tel: +1-314-935-5548; Fax: +1-314-935-5464

E-mail address: pbiswas@wustl.edu

ABSTRACT

Charging in flames significantly affects the properties of the resultant particles produced because of its influence in almost all stages of particle formation. The charging characteristics of flame-generated sub-3 nm particles were investigated with three enhanced particle detectors including a high resolution differential mobility analyzer (DMA) coupled with an electrometer, a particle size magnifier coupled with a butanol-based condensation particle counter (PSM-bCPC), and an atmospheric pressure interface time-of-flight mass spectrometer (APi-TOF). Up to 95% of the flame-generated sub-3 nm particles were charged at a sampling height of 5 mm above the burner, indicating the existence of a strong ionization process in the investigated flame. This high fraction of charged particles contradicts the classical charging theories, which predict < 1% charge fraction for particles below 3 nm. Positively and negatively charged sub-3 nm particles generated from a blank flame were dominated by organic ions and nitrate ions respectively. The flame-generated ions play an important role during titanium dioxide (TiO_2) nanoparticle synthesis, as shown by the attachment of nitrate species on Ti-containing particles observed by the APi-TOF. The effects of the sampling height and precursor feed rate were also investigated.

KEYWORDS: Flame Synthesis, Charge Fraction, Sub-3 nm Particle, Titanium Dioxide, Differential Mobility Analyzer, Mass Spectrometry

1. Introduction

In recent years, the demand for precise control of functional flame-synthesized nanoparticle properties, such as their size, morphology, and crystal phase, has led to a growing interest in studying particle formation mechanisms in high temperature systems. While synthesizing nanoparticles, the flame generates a large amount of ions and charged particles due to the chemical ionization and thermal ionization reactions [1-4]. The existence of these ions makes the flame a quasi-neutral plasma that significantly impacts particle formation and growth processes that eventually determine the properties of the synthesized nanomaterials. The highly concentrated ions and charged species actively collide with the synthesized nanoparticles, affecting the final product due to enhanced coagulation effects [5, 6]. More importantly, the particle nucleation and growth at initial stages are strongly chemistry-dependent [7, 8], and therefore the flame-generated ions and particles may selectively combine with the synthesis precursors and nucleated nanoparticles, producing nanomaterials with undesired or in some instances, tailored contamination. Therefore, the study of particle charging characteristics needs to focus on how the flame-generated ions affect the particle synthesis and what can be done to control these processes.

Much work has been conducted on measuring the charging characteristics of flame-generated nanoparticles. Langmuir probes are often used to determine the total concentration of the charged species in the flames due to their simple design, although the theory can be complex [1, 9, 10]. Condensation particle counters (CPCs) measure total particle concentrations regardless of charging states, and by coupling the CPCs with a charged particle remover (CPR), studies have determined the neutral fractions of flame synthesized particles [11]. Size-resolved particle charge fractions, or charge distributions, are typically determined by using the tandem

differential mobility analyzer (TDMA) method. It utilizes two differential mobility analyzers (DMAs), which classify particles according to their electrical mobility equivalent size, based on the balance between the electrostatic force and drag force [12, 13]. In a TDMA setup, by passing the monomobile particles classified by the first DMA into a charge conditioner and then into a second DMA for mobility scanning, the fractions of particles carrying a specific number of charges can be determined [14, 15]. Theoretical analysis of the particle charging characteristics rely on the Fuchs' charging theory [16] or Boltzmann's charging theory [17], which assumes that particle charging is in a steady state or in equilibrium. Brownian dynamic simulation has been conducted to calculate the steady state-charge distribution on particles with arbitrary shapes [18]. Experimentally measured charge distributions matched quantitatively with the theoretically predicted results in the particle size range between 10 nm and 1000 nm [11, 19].

It should be noted, however, that most of the charging studies, mentioned above, focused on particles larger than 3 nm. Also, the charging of particles in the size ranges of initial stages of formation and growth have not been studied in sufficient detail. This has been partly because of the limitation in available instruments and methods. For example, DMAs suffer from low resolution due to the high diffusivity of the sub-3 nm particles [20], while the activation of sub-3 nm particles in CPCs has always been a difficult problem [21]. Moreover, as the particle size drops below 3 nm, which is comparable to the size of the ions, the particle charging process changes from physical collisions between ions and particles to chemical reactions between the charged and uncharged molecular clusters. Due to the differences in the chemical properties and proton affinities, neutral species can be charged at different efficiencies, which cannot be predicted by the classical charging theories. These limitations hinder a comprehensive

understanding of the particle charging mechanisms, forming a knowledge gap in the formation of particles.

A series of enhanced particle detectors created in recent decades can be valuable tools to study the charging characteristics of sub-3 nm particles. In order to counteract the diffusion broadening of the DMA transfer functions, high resolution DMAs with new configurations or with sheath flow rates over 100 liters per minute (lpm) were designed [22, 23], so that the residence time and diffusional loss of classified particles were significantly reduced. By applying an electrometer downstream of the high resolution DMA, the concentration of the classified sub-3 nm particles can be readily measured [3, 24-29]. Conventional CPCs have been modified in many aspects, which include their working fluid [30], working temperature [31], flow rates [31], and flow pattern [32, 33], to effectively activate the condensational growth of particles below 3 nm. Using diethylene glycol (DEG) as the working fluid, a particle size magnifier (PSM) can grow particles from as small as 1 nm [33] to a size that can be detected by subsequent, conventional butanol CPCs (bCPCs). By scanning the saturation ratio, particles with different sizes are activated and counted, so that the size distributions of the sub-3 nm particles are obtained [34, 35]. Molecular Beam Mass Spectrometry (MBMS) has often been used in studying ion generation in flames, these studies were typically conducted in low pressure and fuel-rich conditions due to the strict requirements of the setup [1]. Limited studies have been conducted in atmospheric pressure CH_4/O_2/Ar flames wherein important chemical ionization reactions have been identified [36-38]. Particle mass spectrometry [39] and transmission electron microscopy of particles collected by molecular beam sampling [40] have also been used for investigating the charging characteristics, growth dynamics, and shapes of incipient soot nanoparticles. The recently developed atmospheric pressure interface time-of-flight mass spectrometer [41] (APi-

TOF, Tofwerk AG) greatly helps determine the chemical composition of the sub-3 nm charged particles in accessible conditions [42]. The combination of the three mentioned enhanced particle detectors (high resolution DMA coupled with an electrometer, PSM-bCPC, and APi-TOF) has served as a powerful tool in understanding the atmospheric particle formation below 3 nm and the role of ions in the atmospheric nucleation [43, 44]. Table 1 is a brief summary of the instruments discussed above for incipient particle measurement including their acronyms and functions.

In this work, three enhanced particle detectors were applied in studying the particle charging characteristics of flame-generated sub-3 nm particles. The total and neutral particle size distributions were measured by the PSM-bCPC, and were compared with the high resolution DMA-measured particle mobility size distributions. The APi-TOF further identified the chemical compositions of the flame-generated sub-3 nm charged particles. This study also investigated the effects of the sampling height, the addition of a synthesis precursor, and the precursor feed rates on the chemical compositions, size distributions, and charging characteristics of the flame-generated sub-3 nm particles.

2. Experimental setups and methods

2.1. Premixed flat flame aerosol reactor

Figure 1 shows a schematic diagram of the experimental setup. A premixed flat flame was used in this study for generating sub-3 nm particles, due to its high stability, one-dimensionality, and broad usage. The combustion mixture consisted of methane (CH_4, > 99.5%, Linde AG) and oxygen (O_2, >99.95%, Linde AG). Nitrogen (N_2, >99.95%, Linde AG) was used to dilute the system and control the flame temperature. A set of mass flow controllers (MKS Inc.)

maintained the total flow rates of CH_4, O_2, and N_2 at 1.00 lpm, 2.85 lpm, and 6.00 lpm, respectively, keeping the flame equivalence ratio at 0.70 (fuel-lean). The stainless steel burner was made of two concentric cylinders with inner and outer diameters of 19 and 25 mm, respectively, forming a gap to provide an extra stream of N_2 with a flow rate of 3 lpm for shielding the flame. The inner cylinder was capped by a honeycomb with a mesh size of 0.5 mm, and was further filled with 2 mm stainless steel beads to maintain laminar flow with a uniform velocity profile at the head of the burner. To study the effects of the addition of a synthesis precursor and precursor feed rates, a bypass flow of N_2 was passed through a bubbler containing titanium isopropoxide (TTIP, Sigma-Aldrich Inc., >97%) at a stable temperature of around 20 ^oC and subsequently fed into the flame. The effect of adding precursors on flame equivalence ratio and flame temperature were minimal because of the low feed rates of the precursors (Table 2). Due to the imperfect design of the burner, the flame does not look entirely flat. The vertical distance from the highest point of the flame to the lowest point of the flame was approximately 3 mm, and the flame height (the distance between the lower side of the flame sheet and the upper side of the burner) was approximately 1 mm. Inside the flame, thermal decomposition, hydrolysis, and combustion of TTIP resulted in the production of titanium dioxide (TiO_2). Previous measurements conducted with a high-resolution DMA have shown that a large quantity of sub-3 nm particles is formed during these processes [3, 20, 45], and the existence of these particles were confirmed by atomic force microscopy (AFM) images of particles collected by thermophoretic sampling [3]. The DMA-measured and AFM-determined particle size distributions matched considerably well in the studied particle size range, indicating the accuracy of the DMA measurement. In order to quench further reactions and particle growth, the sub-3 nm particles were sampled by a radially positioned dilution probe with an inlet diameter of 0.5 mm

at a dilution N_2 flow rate of 24 lpm. The outer diameter of the dilution probe was 8 mm. A dilution ratio of around 200 was reached considering the thermal expansion of the sampled flow. Detailed descriptions of the dilution probe can be found in Wang et al. [45] The sampled sub-3 nm particles were then introduced to the enhanced particle detectors.

2.2. Enhanced particle detectors

This study used a Herrmann-type high resolution DMA (Herrmann DMA) [46, 47], a PSM-bCPC [33], and an APi-TOF [41] to detect the concentration and chemical composition of the sub-3 nm particles.

The Herrmann DMA was operated in a closed loop so that the inlet and outlet sheath flows were balanced. The rate-controllable sheath flow was provided by a brushless blower (DOMEL Inc.), and was further cleaned and cooled by an inline filter and heat radiator. The voltage across the two electrodes of the DMA was applied by a high voltage power supply (Spellman Inc.) controlled by LabVIEW. The DMA measurement used a step voltage of 3 V and a step time of 1 s, which were found to be sufficient for obtaining stable signals. After being classified by the Herrmann DMA, the charged sub-3 nm particles were introduced to an aerosol electrometer (3068B, TSI Inc.) operated at a flow rate of 10 lpm. By assuming that the measured particles carried a single charge, the particle concentration was directly proportional to the current measured by the electrometer (EM). The EM current data were collected by the LabVIEW through RS-232 communication. In the results section, the DMA-measured particle size distributions are represented qualitatively by the EM current as a function of particle size, since the data inversion of the sub-3 nm particles was found to be highly chemistry-dependent [20]. In order to obtain the mobility of the classified particles at each DMA voltage, the

Herrmann DMA was calibrated by the mobility standards generated from the electrosprays of tetra-heptyl ammonium bromide methanol solution (THABr, 99%, Sigma-Aldrich) before the measurements [48]. The measurement accuracy of the Herrmann DMA has been thoroughly characterized in a recent study [47]. The size of the classified particles was further calculated based on the Stokes-Millikan equation and the definition of electrical mobility [17],

$$Z = \frac{eC}{3\pi\mu d_p}, \quad (1)$$

where Z is the particle electrical mobility, e is the electronic charge, C is the slip correction factor, μ is the air viscosity, and d_p is the mobility diameter of the particle. Existing studies suggest that the volumetric diameter (d_v) of a sub-3 nm particle can be approximated by subtracting d_p by 0.3 nm, which is the gas molecule's effective diameter [49]. Further calculation is also needed to derive the exact value of the particle mobility diameter, since the influence of the ion-induced dipole potential on the particle mobility is not evaluated in the Stokes-Millikan equation for sub-3 nm particles [49, 50]. However, for simplicity, the mobility diameter of the particle calculated by Eq. (1) was used to evaluate the particle size distributions.

The PSM-bCPC measured the sub-3 nm particle size distributions based on the size-dependent particle activation. Sub-3 nm particles were first grown by the PSM in an environment of supersaturated DEG vapors, and then introduced to a bCPC for further growth and optical detection. Details about the theory and operation can be found elsewhere [33, 35]. The PSM detection efficiency was calibrated using the positively charged particles generated in the flame. Conditions of the blank flame and with TTIP addition were calibrated separately to obtain different calibration curves. These curves were then used separately for interpreting the PSM data. Due to the fact that different species of particles were observed in positively charged,

negatively charged, and neutral particles, uncertainty exists in the PSM-obtained particle number concentrations and charge fractions. Furthermore, existing studies suggested that neutral particles are less easy to activate due to the missing of ion-induced dipole effects [5, 6, 49, 50].However, a recent study has revealed that heterogeneous nucleation does not clearly favor particles with certain charging states, while the chemical composition of the sub-3 nm particles plays a more important role [51]. In this study, the PSM-bCPC (Model A11, Airmodus Oy) was used to determine the charge distributions of the sub-3 nm particles. Teflon tubing is widely found to significantly remove ions and charged particles due to the electric field built at the inner surface of the tube, and this property makes it a convenient and efficient charged particle remover (CPR). This charge-removing effect can be achieved with a very short section of the tube (a few centimeters), since the mean surface electric field for the Teflon tubing can be in the range of 50-200 V/cm [52]. This charge-removing effect is significantly suppressed by using conductive tubing for aerosol sampling. A 6.0 mm-wide, 10 cm-long Teflon tubing or conductive silicone tubing was initiated before the PSM-bCPC, so that both the neutral and total particle size distributions can be measured. The same length of tubes could guarantee the same amount of diffusion loss in the tubes. The charge distribution of the flame-generated sub-3 nm particles were then calculated by comparing the size distributions obtained with different tubes.

The chemical composition of the flame-generated charged particles was obtained by directly feeding the sample aerosols to the APi-TOF. The APi-TOF could achieve a mass resolving power of 3000 Th/Th and a mass accuracy of 0.002%. The spectra were further analyzed with tofTools (a MATLAB®-based set of programs) [53], where the accurate mass and isotope distributions determined the exact species of the charged particles. To better analyze incipient clusters with similar chemical compositions, a mass defect plot was created which uses

measured ion mass plotted on the x-axis and mass defect against nominal mass (integer mass) on the y-axis [41]. For example, since carbon has an atomic mass of 12.0000 (nominal mass of 12) and hydrogen has an atomic mass of 1.0078 (nominal mass of 1), C_nH_n clusters will have a mass defect of +0.0078*n*. By plotting C_nH_n clusters in a mass defect plot, one can get a straight line with a slope of +0.0078/(12+1.0078). In a mass defect plot, each section of straight lines represents species spaced by a same molecular composition. The mass defect plot can further help in understanding the conversion and reaction of the species. The "Kendrick mass defect spectrum" is based on this idea where both the x-axis and y-axis are scaled to assist the analysis of grouped hydrocarbons [54].

The particle residence times in the sampling lines were approximately 12 ms, 52 ms, 9 ms, and 30 ms, for the sections from the dilution sampler inlet to the DMA inlet, from the dilution sampler inlet to the PSM-bCPC inlet, from the dilution sampler inlet to the APi-TOF inlet, and from the DMA outlet to the EM inlet, respectively. However, the particle loss in the system took place dominantly in the instruments. For example, the transmission efficiencies of particles in the APi-TOF and the DMA were estimated to be 0.1 to 0.5% and 1 to 22%, respectively, depending on the setting of the instruments [41, 47]. Due to the difficulty for calibrating the particle transmission efficiencies, the particle loss was not evaluated. It should be noted that sampling in a flame with a probe will inevitably alter a sample. Although it has been carefully calibrated, the dilution sampler used in this study may not be sufficient to quench all reactions and particle dynamics. A recent study by Carbone et al. [24] shows that measuring sub 3 nm soot particles with dilution samplThaers is very challenging, since the critical conditions for suppressing particle coagulation and charge distribution were not achieved even at a dilution ratio of 6.2×10^3. Existing studies also suggested that an adequate dilution ratio larger than 10^4 is

typically required so that the obtained particle size distributions are "asymptotic" [55]. Furthermore, the rapid cooling of the sample may also impact the complex state of vapor-cluster balance in the flame, and cause alteration of the incipient particle measurement [38, 56, 57]. Hence, there is a small chance that the observed incipient particles might not have been formed in the flame and are not reflective accurately of flame species.

2.3. Experimental plan

Eleven sets of experiments (Table 2) were designed to study the effects of the sampling height, addition of synthesis precursor (TTIP), and precursor feed rates on the charging characteristics of flame-generated sub-3 nm particles. Tests 1 to 4 were conducted without TTIP addition to study the effect of sampling height on the particles generated from blank flames. Tests 5 to 11 investigated the effect of TTIP feed rates and sampling height during TiO_2 synthesis. The sampling height (H_{AB}) was the vertical distance from the head of the burner to the inlet of the dilution sampler. The TTIP feed rate was calculated based on the saturation vapor pressure of TTIP in N_2 presented by Siefering and Griffin [58].

3. Results and discussion

3.1. Sub-3 nm particles generated from a blank flame

Figure 2 shows the PSM-measured size distribution of particles generated from the blank flame at a sampling height of 5 mm. The neutral particle size distribution was also measured, which is not distinguishable in the graph, indicating a minimal formation of neutral particles in this condition. This result also explained the qualitative match between the shapes of the PSM and DMA-measured size distributions below 3 nm, because the DMA classified charged

particles only. A large amount of charged clusters below 1.5 nm were generated from the blank flame, which was also observed in previous studies [3, 20]. These charged particles were generally believed to come from the intensive chemical ionization and thermal ionization during combustion [1]. During CH_4 combustion, the chemically produced positively and negatively charged species mainly come from the reactions

$$CH + O \rightarrow CHO^+ + e^-, \text{ and} \quad (2)$$

$$CH^* + C_2H_2 \rightarrow C_3H_3^+ + e^-, \quad (3)$$

where the formed ions and electrons may collide with other molecules to form more stable charged species [59]. According to recent work by Jones and Hayhurst [38], reaction shown in Eq. (2) dominates more oxygen-rich flames of methane (C/O ≤ 0.4). A pool of positive ions is then formed rapidly, mainly through proton transfer from CHO^+ to other intermediates and final products of combustion. Previous measurements with Langmuir probes and MBMS determined that the concentration of ions produced by chemical ionization in flames can be as high as 10^{11}#/cm^3 [19, 38, 60]. An estimation of ion concentration in this investigated flame was also conducted, and the ion concentration was approximately 10^{10}#/cm^3 (supplementary content). This value is close to the those obtained in the work of Jones and Hayhurst [38]. The effect of thermal ionization can be briefly evaluated by Saha's equation, where the equilibrium concentrations of thermally ionized charged species can be calculated by

$$K = \frac{n_+ \cdot n_e}{n} = G\left(\frac{2\pi m_e kT}{h^2}\right)\exp\left(-\frac{A_I}{kT}\right), \quad (4)$$

where K is the equilibrium constant, n_+, n_e, and n are the concentrations of the positively charged species, electrons, and neutral particles. G is defined as $g_+ \cdot g_e / g$, where g_+, g_e, and g are the statistical weights of an ion, electron, and neutral particle, respectively. m_e is the

electron mass, k is Boltzmann's constant, T is temperature (a value of 2200 K is used), and h is Plank's constant. A_I is the ionization potential of the species, which is typically larger than 10 eV in a fuel-lean flame [61]. The calculated value of K was below 10^{-12} #/m^3, indicating a minimal effect of thermal ionization in this studied flame. Hence, we could conclude that most of these ions were coming from the chemical ionization in the flame.

The DMA-measured size distributions (Fig. 2) demonstrates that positively charged particles had larger averaged mobility sizes (lower electrical mobilities) than negatively charged particles, which is common in ionization sources [62]. The inverse mobilities are labeled in the upper x-axis of Fig. 2 as a reference. A possible explanation for the difference in the average mobilities between the polarities is that chemical ionization reactions produce relatively large organic particles as positive charge carriers, while electrons are the dominant negative charge carrier. These free electrons can further attach on other species with smaller mobility sizes to generate negative ions at atmospheric pressure [38, 63, 64] through

$$HX + e^- \rightarrow H + X^- . \quad (5)$$

Through this reaction, major negative ions, such as C_2H^- and OH^-, or halogen ions, can be generated [38, 64]. According to Fuchs theory, the difference in the electrical mobility may cause a higher fraction of particles to carry negative charges, since the more mobile negatively charged clusters may collide with neutral particles more frequently. It should also be noted that the measured ion mobilities were higher than those obtained in sooting flames (~ 1 cm^2/Vs), where larger clusters of unsaturated carbon clusters were formed [1].

Figure 3 displays the effect of sampling height on the PSM-measured particle size distributions and neutral particle fractions. As the probe height (H_{AB}) increased, a minor decrease in the particle concentration was observed (Fig. 3a), which could be explained by the formation

of neutral particles by ion recombination above the flame sheet. One should notice that the concentration of sub-3 nm particles at different H_{AB} were still in similar orders of magnitude, implying a relatively long age (>10 ms) of the generated particles. The neutral fraction of sub-3 nm particles was very low (< 10%, Fig. 3b), and as the residence time increased (higher H_{AB}), the recombination of ions did not have a significant effect on the neutral fractions. The neutral particle fraction was far from the theory-predicted values of around 100% for particles below 10 nm, indicating that a large fraction of particles were charged in this size range during combustion. Furthermore, the neutral fraction of 1.29 nm particles was always higher than that of 1.17 nm particles (Fig. 3b), contradicting the classical charging theories which predict a lower charging probability of particles with smaller sizes. This large discrepancy may be caused by the chemical ionization which produces positive ions with different sizes as stated earlier, and may also be a result of the unsteady charging process, which is not considered in classical charging theories. This feature requires additional experimental work.

The mass spectra of the positively and negatively charged sub-3 nm particles are shown in Fig. 4. The spectra of the positive particles contained a lot of hydrocarbons peaks, which complicated the identification of the ion species (Fig. 4a). Possible compositions of the major peaks were $C_4H_{11}O_3^+$ (107.0708 Da), $CH_{16}O_6^+$ (120.0634 Da), $C_{14}H_{30}N^+$ (212.2378 Da), and $C_{15}H_{32}ON^+$ (242.2487 Da). Unfortunately, the chemical structure of these charged clusters cannot be deciphered. Future work will be attempted to analyze the chemical structures and locate functional groups of these clusters, so that more information can be derived for incipient particle formation. The inset figure shows the mass defect plot of the positively charged particles, with the fitted line displaying the mass defects of particles with a chemical formula of C_nH_n. The match between most of the data points and the fitted line indicates that the formed positively

charged sub-3 nm particles were mainly composed of unsaturated hydrocarbons. It is also possible that the formation of polycyclic aromatic hydrocarbons (PAH) took place during the combustion of methane [65, 66]. These detected species are important intermediates during particle formation due to their high abundance. Furthermore, they can provide the surface area for particle condensation and coagulation growth. It is interesting that the detected major species (such as $C_4H_{11}O_3^+$ and $CH_{16}O_6^+$) did not fall on the fitted mass defect line, which requires more effort to explain this phenomenon. The negatively charged clusters were mostly composed of nitrate ions. Major peaks of NO_3^- (61.9878 Da), $HNO_3NO_3^-$ (124.9835 Da), and $(HNO_3)_2NO_3^-$ (187.9791 Da) were detected and confirmed by the highly resolved atomic masses and isotope distributions. The existence of nitrogen-containing species might be a result of NO_x formation, especially when the flame was operated in a fuel-lean condition which favors NO_x production. Further, the electrons and water produced by combustion might react with NO_x to generate nitrate ions, which were also found to be the dominant ions in other types of ionization sources such as radioactive neutralizers [62, 67] and corona dischargers [68]. Due to its high concentration, the nitrate ions were very likely to participate in the charging of sub-3 nm particles during particle synthesis, as discussed in the following section.

3.2. Sub-3 nm particles generated during flame synthesis of TiO_2

After TTIP was introduced to the flame, particles with mobility sizes larger than 1.5 nm were detected by both the PSM-bCPC and DMA (Fig. 5). This increase in size was a result of particle nucleation and growth at the initial stages. The neutral particle concentrations also increased compared to the blank flame conditions, although the neutral fraction was still low (~ 5%

at H_{AB} = 5 mm). Due to the large fraction of the charged particles, DMA-measured particle size distributions again matched well with the PSM-measured total particle size distributions. Separate peaks between 1 nm and 1.25 nm were detected in the DMA-measured particle size distributions, indicating the formation of some stable particles during the synthesis of TiO_2 [3]. These stable particles may act as important intermediates during the formation of TiO_2. Again, positively charged particles had larger averaged mobility sizes than the negatively charged particles.

The chemical compositions of the sub-3 nm charged particles were analyzed with the APi-TOF, and the mass spectra are displayed in Fig. 6. A significant number of peaks was detected in both polarities. The existence of titanium elements in the particles was confirmed with the high-accuracy mass and the titanium isotope distribution (^{48}Ti: 73.7%; ^{46}Ti: 8.3%; ^{47}Ti: 7.4%; ^{49}Ti: 5.4%; ^{50}Ti: 5.2%). The identified peaks are represented in Fig. 6 and listed in Table 3. Classical nucleation theories [22] predicted that a TiO_2 single molecule could serve as a stable monomer due to its low saturation vapor pressure; however, pure TiO_2 particles were not detected by the mass spectrometer. A major peak of $Ti(OH)_4H^+$ was found in the positively charged particles, which agreed with the TTIP reaction pathways in a $H_2/O_2/Ar$ premixed flame proposed by Shmakov et al. [69] Similar species were also observed in a fuel-rich C_2H_2/O_2 premixed flame with the addition of atomized droplets of $TiCl_4$ aqueous solution [70]. Other identified positively charged species typically contained unreacted hydrocarbons from TTIP propanol groups, indicating the necessity for future controlled experiments studying ion generation from propanol flames. As for negatively charged species, the nitrate ions played an important role in the formation of sub-3 nm particles. The APi-TOF detected a series of titanium and nitrate-containing particles, for example, $TiO_4(NO_3)_2^-$ at m/z of 235.9032 Th, $TiO_2(NO_3)_3^-$ at

m/z of 265.9012 Th, and $Ti_2O_8(NO_3)_2^-$ at m/z of 347.8308 Th, etc. The detected compositions indicate that, in molecular clusters, titanium has preferable oxidation states other than +4. This may demonstrate a strong interaction between the flame-generated ions and the synthesized materials, where the flame-generated ions were actively consumed during the particle formation at initial stages. This scavenging effect also explains the increase of neutral particle fraction observed in Fig. 5. It is also possible that the precursor molecule, TTIP may become readily ionized in the flame, serving as the seed for further particle growth. It should be noted that the flame-generated ions in the sub-3 nm particles might serve as contaminants for the further growth of particles and may affect crystallization. Therefore, it would be worthwhile to conduct similar measurements in systems without the presence of hydrocarbon and nitrate species, such as in $H_2/O_2/Ar$ flames, in order to study the effect of organic and nitric ions on particle formation and growth. A recent study has shown that pure tungsten oxide clusters can be detected through the measurement with molecular beam mass spectrometry in an $H_2/O_2/Ar$ flame at low pressures. However, since flame synthesis is mainly conducted with the participation of N_2, and due to safety considerations and cost-effectiveness, hydrocarbons are commonly used as fuels, further work investigating the role of nitrate and hydrocarbon species in the particle growth and crystallization processes is still needed.

The mass defect plots of the positively and negatively charged particles are displayed as insets in Fig. 6. Most of the negatively charged particles fell on the straight line representing the mass defects of particles containing NO_3 as the core and TiO_2NO_3 as the additional group. The mass defect plot of the positively charged particles shows some interesting properties. Detected particles had a major trend of decreasing mass defects as the atomic mass increased because of the addition of titanium and oxygen, which have negative mass defects, i.e., exact atomic mass of

47.9479 and 15.9949, respectively. However, the whole mass defect plot was composed of separate segments where the mass defect was increasing with atomic mass, possibly contributed by the existing hydrocarbons, since hydrogen has a positive mass defect (exact mass of 1.0078). These segments indicate the presence of dehydrogenation and dehydration during the precursor reaction. The different patterns of the mass defect plot clearly suggest the presence of different reaction regimes during the formation of TiO_2 particles. Apart from the cluster mobility and mass spectrum, the mass and mobility information of specific molecular cluster is also of great interest, since it can reveal critical information on the structure of these molecular clusters, such as collision cross section area, atom arrangement, etc [29]. However, in order to obtain the particle mobility and mass simultaneously, a tandem arrangement of the DMA and mass spectrometer, and more complex data analysis are required, which can be found in a recent study of the same group [4].

3.3. Effect of precursor feed rate and sampling height

Due to the scavenging of flame-generated ions by the synthesized materials, one would expect a positive correlation between the neutral particle fraction and the precursor feed rate. Figure 7 shows the PSM-measured size distributions and neutral particle fractions as a function of the precursor feed rate. It was observed that when H_{AB} = 5 mm, particles larger than 1.5 nm were formed, while smaller particles at around 1.1 nm were first generated and then consumed, due to the enhanced coagulation and continue particle growth (Fig. 7a). The neutral particle fraction indeed increased with the TTIP feed rate, reaching around 10% with a precursor feed rate of 0.213 mmol/hr where H_{AB} = 5 mm, confirming the strong interaction between the flame-generated ions and the synthesized particles.

Unlike the case for the blank flame-generated ions (Fig. 4), sampling height significantly changed the size distribution and neutral fraction of particles formed from the flame with precursor addition. At a precursor feed rate of 0.213 mmol/hr, the particle size distribution shifted from 1.1 nm to 2.25 nm as sampling height increased (Fig. 7a). The neutral fraction also greatly increased, approaching around 90% when the sampling height was 20 mm. The neutral fractions of 1.17 nm and 1.29 nm particles were 53.8±11.2 % and 56.8±13.4 % at H_{AB}=10 mm, and 88.9±7.1 % and 82.3±18.3 % at H_{AB}=20 mm. This large difference in the charge fraction is attributed to the existence of particles with larger sizes. The ions produced by the chemical ionization in the flame randomly collided with and attach onto particles formed from *TTIP* reaction. Particles with larger sizes possessed larger cross-sectional areas (and coagulation sink [71]), facilitating the recombination and neutralization of the system. This effect might have also been maximized, due to the small size scale of this charging process. Still, the neutral particle fractions were far from the theoretically predicted values, indicating a need for analytically studying the time-dependent charging mechanisms in the flame [2].

4. Conclusions

With the help of three enhanced particle detectors, the charging characteristics of sub-3 nm flame-generated particles were studied for the first time (to the best of our knowledge). The PSM-bCPC and high resolution DMA matched qualitatively well in measuring the sub-3 nm particle size distributions. Coupled with a CPR, the PSM-bCPC measured the neutral particle size distributions during combustion, and the neutral particle fraction in the flame was found to be significantly lower than predicted by classical theory. The APi-TOF provided the chemical compositions of the sub-3 nm charged species. Under blank flame conditions, the positively

charged particles were mainly composed of hydrocarbons, while nitrate ions dominated the negatively charged particles. NO_x formation was considered to be the major reason for generating nitrate species. A strong interaction between the flame-generated ions and synthesized materials was observed, which was indicated by the existence of nitrate species in the Ti-containing particles. The appearance of these ion species might further affect the quality of the final synthesized product. The formation of particles during combustion consumed the flame-generated ions, which further increased the neutral particle fraction in the flame. Flame-generated ions play an important role during the particle formation at the initial stages. New perspectives on synthesizing functional nanomaterials through combustion may be obtained through changing the ion characteristics in flame environments.

Acknowledgements

This work is supported by the Solar Energy Research Institute for India and the United States (SERIIUS), funded jointly by the U.S. Department of Energy (Office of Science, Office of Basic Energy Sciences, and Energy Efficiency and Renewable Energy, Solar Energy Technology Program, under Subcontract DE-AC36-08GO28308 to the National Renewable Energy Laboratory, Golden, Colorado) and the Government of India, through the Department of Science and Technology under Subcontract IUSSTF/JCERDC-SERIIUS/2012. The work was also supported by Academy of Finland via Center of Excellence project in Atmospheric Sciences (272041) and European Commission via ACTRIS2 (654109). Y.W. thanks Mr. Adewale Adeosun at Washington University in St. Louis for the helpful discussion.

References

[1] A.B. Fialkov, Investigations on ions in flames, Prog. Energy Combust. Sci. 23 (1997) 399-528.
[2] J. Jiang, M.-H. Lee, P. Biswas, Model for nanoparticle charging by diffusion, direct photoionization, and thermionization mechanisms, J. Electrostat. 65 (2007) 209-220.
[3] J. Fang, Y. Wang, M. Attoui, T.S. Chadha, J.R. Ray, W.-N. Wang, Y.-S. Jun, P. Biswas, Measurement of sub-2 nm clusters of pristine and composite metal oxides during nanomaterial synthesis in flame aerosol reactors, Anal. Chem. 86 (2014) 7523-7529.
[4] Y. Wang, J. Kangasluoma, M. Attoui, J. Fang, H. Junninen, M. Kulmala, T. Petäjä, P. Biswas, Observation of incipient particle formation during flame synthesis by tandem differential mobility analysis-mass spectrometry (DMA-MS), Proc. Combust. Inst. (2016). http://dx.doi.org/10.1016/j.proci.2016.07.005.
[5] M. Adachi, M. Kusumi, S. Tsukui, Ion-induced nucleation in nanoparticle synthesis by ionization chemical vapor deposition, Aerosol Sci. Technol. 38 (2004) 496-505.
[6] Y. Zhang, S. Li, W. Yan, Q. Yao, D.T. Stephen, Role of dipole–dipole interaction on enhancing Brownian coagulation of charge-neutral nanoparticles in the free molecular regime, The Journal of chemical physics 134 (2011) 084501.
[7] J. Kangasluoma, C. Kuang, D. Wimmer, M. Rissanen, K. Lehtipalo, M. Ehn, D. Worsnop, J. Wang, M. Kulmala, T. Petäjä, Sub-3 nm particle size and composition dependent response of a nano-CPC battery, Atmos. Meas. Tech. 7 (2014) 689-700.
[8] J. Kirkby, J. Curtius, J. Almeida, E. Dunne, J. Duplissy, S. Ehrhart, A. Franchin, S. Gagné, L. Ickes, A. Kürten, Role of sulphuric acid, ammonia and galactic cosmic rays in atmospheric aerosol nucleation, Nature 476 (2011) 429-433.
[9] J. Guo, J.M. Goodings, A.N. Hayhurst, S.G. Taylor, A simple method for measuring positive ion concentrations in flames and the calibration of a nebulizer/atomizer, Combust. Flame 133 (2003) 335-343.
[10] I. Langmuir, H. Mott-Smith, Langmuir probe technique, Gen. Elec. Rev 27 (1924) 449.
[11] M. Sahu, J. Park, P. Biswas, In Situ Charge Characterization of TiO_2 and Cu-TiO_2 Nanoparticles in a Flame Aerosol Reactor, J. Nanopart. Res. 14 (2012) 1-11.
[12] E. Knutson, K. Whitby, Aerosol classification by electric mobility: apparatus, theory, and applications, J. Aerosol Sci. 6 (1975) 443-451.
[13] X. Ma, C. Zangmeister, M. Zachariah, Soot oxidation kinetics: a comparison study of two tandem ion-mobility methods, J. Phys. Chem. C 117 (2013) 10723-10729.
[14] M. Attoui, M. Paragano, J. Cuevas, J. Fernandez de la Mora, Tandem DMA generation of strictly monomobile 1–3.5 nm particle standards, Aerosol Sci. Technol. 47 (2013) 499-511.
[15] M. Maricq, Size and charge of soot particles in rich premixed ethylene flames, Combust. Flame 137 (2004) 340-350.
[16] N. Fuchs, On the stationary charge distribution on aerosol particles in a bipolar ionic atmosphere, Geofisica pura e applicata 56 (1963) 185-193.
[17] S.K. Friedlander, Smoke, dust, and haze: fundamentals of aerosol behavior, Oxford University Press New York, USA, 2000.
[18] R. Gopalakrishnan, M.J. Meredith, C. Larriba-Andaluz, C.J. Hogan Jr, Brownian dynamics determination of the bipolar steady state charge distribution on spheres and non-spheres in the transition regime, J. Aerosol Sci. 63 (2013) 126-145.

[19] S. Kim, K. Woo, B. Liu, M. Zachariah, Method of measuring charge distribution of nanosized aerosols, J. Colloid Interface Sci. 282 (2005) 46-57.
[20] Y. Wang, J. Fang, M. Attoui, T.S. Chadha, W.-N. Wang, P. Biswas, Application of Half Mini DMA for sub 2 nm particle size distribution measurement in an electrospray and a flame aerosol reactor, J. Aerosol Sci. 71 (2014) 52-64.
[21] K. Iida, M.R. Stolzenburg, P.H. McMurry, Effect of working fluid on sub-2 nm particle detection with a laminar flow ultrafine condensation particle counter, Aerosol Sci. Technol. 43 (2009) 81-96.
[22] J. Fernández de la Mora, J. Kozlowski, Hand-held differential mobility analyzers of high resolution for 1-30nm particles: Design and fabrication considerations, J. Aerosol Sci. 57 (2013) 45-53.
[23] J. Fernandez de la Mora, High-Resolution Mobility Analysis of Charge-Reduced Electrosprayed Protein Ions, Anal. Chem. 87 (2015) 3729-3735.
[24] F. Carbone, M. Attoui, A. Gomez, Challenges of measuring nascent soot in flames as evidenced by high resolution differential mobility analysis, Aerosol Science and Technology 50 (2016) 740-757.
[25] L.A. Sgro, A. D'Anna, P. Minutolo, Charge fraction distribution of nucleation mode particles: New insight on the particle formation mechanism, Combust. Flame 158 (2011) 1418-1425.
[26] L. Sgro, A. Barone, M. Commodo, A. D'Alessio, A. De Filippo, G. Lanzuolo, P. Minutolo, Measurement of nanoparticles of organic carbon in non-sooting flame conditions, Proc. Combust. Inst. 32 (2009) 689-696.
[27] L. Sgro, A. De Filippo, G. Lanzuolo, A. D'Alessio, Characterization of nanoparticles of organic carbon (NOC) produced in rich premixed flames by differential mobility analysis, Proc. Combust. Inst. 31 (2007) 631-638.
[28] L.A. Sgro, A. D'Anna, P. Minutolo, Charge distribution of incipient flame-generated particles, Aerosol Sci. Technol. 44 (2010) 651-662.
[29] H. Ouyang, S. He, C. Larriba-Andaluz, C.J. Hogan Jr, IMS-MS and IMS-IMS Investigation of the Structure and Stability of Dimethylamine-Sulfuric Acid Nanoclusters, J. Phys. Chem. A 119 (2015) 2026-2036.
[30] D. Wimmer, K. Lehtipalo, A. Franchin, J. Kangasluoma, F. Kreissl, A. Kürten, A. Kupc, A. Metzger, J. Mikkilä, T. Petäjä, Performance of diethylene glycol based particle counters in the sub 3 nm size range, Atmos. Meas. Tech 6 (2013) 1793-1804.
[31] C. Kuang, M. Chen, P.H. McMurry, J. Wang, Modification of laminar flow ultrafine condensation particle counters for the enhanced detection of 1 nm condensation nuclei, Aerosol Sci. Technol. 46 (2012) 309-315.
[32] L.A. Sgro, J. Fernández de la Mora, A simple turbulent mixing CNC for charged particle detection down to 1.2 nm, Aerosol Sci. Technol. 38 (2004) 1-11.
[33] J. Vanhanen, J. Mikkilä, K. Lehtipalo, M. Sipilä, H. Manninen, E. Siivola, T. Petäjä, M. Kulmala, Particle size magnifier for nano-CN detection, Aerosol Sci. Technol. 45 (2011) 533-542.
[34] K. Lehtipalo, J. Leppä, J. Kontkanen, J. Kangasluoma, A. Franchin, D. Wimmer, S. Schobesberger, H. Junninen, T. Petäjä, M. Sipilä, Methods for determining particle size distribution and growth rates between 1 and 3 nm using the Particle Size Magnifier, Boreal Environ. Res. 19 (2014) 215-236.

[35] J. Kangasluoma, M. Attoui, H. Junninen, K. Lehtipalo, A. Samodurov, F. Korhonen, N. Sarnela, A. Schmidt-Ott, D. Worsnop, M. Kulmala, Sizing of neutral sub 3nm tungsten oxide clusters using Airmodus Particle Size Magnifier, J. Aerosol Sci. 87 (2015) 53-62.
[36] J. Goodings, D. Bohme, C.-W. Ng, Detailed ion chemistry in methane-oxygen flames. I. Positive ions, Combust. Flame 36 (1979) 27-43.
[37] J. Goodings, D. Bohme, C.-W. Ng, Detailed ion chemistry in methane-oxygen flames. II. Negative ions, Combust. Flame 36 (1979) 45-62.
[38] H.R. Jones, A.N. Hayhurst, Measurements of the concentrations of positive and negative ions along premixed fuel-rich flames of methane and oxygen, Combust. Flame 166 (2016) 86-97.
[39] H. Mätzing, W. Baumann, H. Bockhorn, H.-R. Paur, H. Seifert, Detection of electrically charged soot particles in laminar premixed flames, Combust. Flame 159 (2012) 1082-1089.
[40] A. Fialkov, A. Hayhurst, S. Taylor, S. Newcomb, Shapes of soot particles, both charged and uncharged, after molecular beam sampling a premixed oxyacetylene flame, burning at atmospheric pressure, Combust. Sci. Technol. 185 (2013) 1762-1776.
[41] H. Junninen, M. Ehn, T. Petäjä, L. Luosujärvi, T. Kotiaho, R. Kostiainen, U. Rohner, M. Gonin, K. Fuhrer, M. Kulmala, A high-resolution mass spectrometer to measure atmospheric ion composition, Atmos. Meas. Tech. 3 (2010) 1039-1053.
[42] M. Kulmala, J. Kontkanen, H. Junninen, K. Lehtipalo, H.E. Manninen, T. Nieminen, T. Petäjä, M. Sipilä, S. Schobesberger, P. Rantala, Direct observations of atmospheric aerosol nucleation, Science 339 (2013) 943-946.
[43] S. Schobesberger, H. Junninen, F. Bianchi, G. Lönn, M. Ehn, K. Lehtipalo, J. Dommen, S. Ehrhart, I.K. Ortega, A. Franchin, Molecular understanding of atmospheric particle formation from sulfuric acid and large oxidized organic molecules, PNAS 110 (2013) 17223-17228.
[44] J. Almeida, S. Schobesberger, A. Kürten, I.K. Ortega, O. Kupiainen-Määttä, A.P. Praplan, A. Adamov, A. Amorim, F. Bianchi, M. Breitenlechner, Molecular understanding of sulphuric acid-amine particle nucleation in the atmosphere, Nature 502 (2013) 359-363.
[45] Y. Wang, P. Liu, J. Fang, W.-N. Wang, P. Biswas, Kinetics of sub-2 nm TiO_2 particle formation in an aerosol reactor during thermal decomposition of titanium tetraisopropoxide, J. Nanopart. Res. 17 (2015) 1-13.
[46] W. Herrmann, T. Eichler, N. Bernardo, J. Fernández de la Mora, Turbulent transition arises at Re 35000 in a short Vienna type DMA with a large laminarizing inlet, Annual Conference of the AAAR, St. Louis, MO, 2000, pp. 6-10.
[47] J. Kangasluoma, M. Attoui, F. Korhonen, L. Ahonen, E. Siivola, T. Petäjä, Characterization of a Herrmann type high resolution differential mobility analyzer, Aerosol Sci. Technol. 50 (2016) 222-229.
[48] S. Ude, J.F. De la Mora, Molecular monodisperse mobility and mass standards from electrosprays of tetra-alkyl ammonium halides, J. Aerosol Sci. 36 (2005) 1224-1237.
[49] C. Larriba, C.J. Hogan Jr, M. Attoui, R. Borrajo, J.F. Garcia, J.F. de la Mora, The mobility-volume relationship below 3.0 nm examined by tandem mobility-mass measurement, Aerosol Sci. Technol. 45 (2011) 453-467.
[50] B.K. Ku, J.F. de la Mora, Relation between electrical mobility, mass, and size for nanodrops 1-6.5 nm in diameter in air, Aerosol Science and Technology 43 (2009) 241-249.
[51] J. Kangasluoma, A. Samodurov, M. Attoui, A. Franchin, H. Junninen, F. Korhonen, T. Kurtén, H. Vehkamäki, M. Sipilä, K. Lehtipalo, Heterogeneous Nucleation onto Ions and Neutralized Ions: Insights into Sign-Preference, J. Phys. Chem. C 120 (2016) 7444-7450.

[52] B. Liu, D. Pui, K. Rubow, W. Szymanski, Electrostatic effects in aerosol sampling and filtration, Ann. Occup. Hyg. 29 (1985) 251-269.
[53] H. Junninen, Data cycle in atmospheric physics: From detected millivolts to understanding the atmosphere, Department of Physical Sciences, University of Helsinki, Helsinki, 2014.
[54] C.A. Hughey, C.L. Hendrickson, R.P. Rodgers, A.G. Marshall, K. Qian, Kendrick mass defect spectrum: a compact visual analysis for ultrahigh-resolution broadband mass spectra, Anal. Chem. 73 (2001) 4676-4681.
[55] B. Zhao, Z. Yang, J. Wang, M.V. Johnston, H. Wang, Analysis of soot nanoparticles in a laminar premixed ethylene flame by scanning mobility particle sizer, Aerosol Sci. Technol. 37 (2003) 611-620.
[56] N.A. Burdett, A.N. Hayhurst, Hydration of gas-phase ions and the measurement of boundary-layer cooling during flame sampling into a mass spectrometer, J. Chem. Soc., Faraday Trans. 78 (1982) 2997-3007.
[57] A. Hayhurst, Mass spectrometric sampling of a flame, Combust. Explos. Shock Waves 48 (2012) 516-525.
[58] K. Siefering, G. Griffin, Growth kinetics of CVD TiO_2: influence of carrier gas, J. Electrochem. Soc. 137 (1990) 1206-1208.
[59] H. Calcote, 8th International Symposium on Combustion, Williams and Wilkins, Baltimore, (1962) 184.
[60] J.M. Goodings, J. Guo, A.N. Hayhurst, S.G. Taylor, Current-voltage characteristics in a flame plasma: analysis for positive and negative ions, with applications, Int. J. Mass Spectrom. 206 (2001) 137-151.
[61] H. Calcote, Mechanisms for the formation of ions in flames, Combust. Flame 1 (1957) 385-403.
[62] A. Maißer, J.M. Thomas, C. Larriba-Andaluz, S. He, C.J. Hogan, The mass-mobility distributions of ions produced by a Po-210 source in air, J. Aerosol Sci. 90 (2015) 36-50.
[63] A. Hayhurst, D. Kittelson, The positive and negative ions in oxy-acetylene flames, Combust. Flame 31 (1978) 37-51.
[64] S. Axford, A. Hayhurst. Mass spectrometric sampling of negative ions from flames of hydrogen and oxygen: the kinetics of electron attachment and Detachment in Hot Mixtures of H_2O, O_2, OH and HO_2. In: editor^editors. Proceedings of the Royal Society of London A: Mathematical, Physical and Engineering Sciences; 1996: The Royal Society. p. 1007-1033.
[65] C.K. Law, Combustion physics, Cambridge University Press2006.
[66] S.R. Turns, An introduction to combustion, McGraw-Hill New York1996.
[67] G. Steiner, T. Jokinen, H. Junninen, M. Sipilä, T. Petäjä, D. Worsnop, G.P. Reischl, M. Kulmala, High-Resolution Mobility and Mass Spectrometry of Negative Ions Produced in a 241Am Aerosol Charger, Aerosol Sci. Technol. 48 (2014) 261-270.
[68] H. Manninen, A. Franchin, S. Schobesberger, A. Hirsikko, J. Hakala, A. Skromulis, J. Kangasluoma, M. Ehn, H. Junninen, A. Mirme, Characterisation of corona-generated ions used in a Neutral cluster and Air Ion Spectrometer (NAIS), Atmos. Meas. Tech. 4 (2011) 2767-2776.
[69] A. Shmakov, O. Korobeinichev, D. Knyazkov, A. Paletsky, R. Maksutov, I. Gerasimov, T. Bolshova, V. Kiselev, N. Gritsan, Combustion chemistry of Ti (OC3H7)4 in premixed flat burner-stabilized H2/O2/Ar flame at 1atm, Proc. Combust. Inst. 34 (2013) 1143-1149.
[70] J.M. Goodings, Q. Tran, N.S. Karellas, Ion chemistry of transition metals in hydrocarbon flames. II. Cations of Sc, Ti, V, Cr, and Mn, Can. J. Chem. 66 (1988) 2219-2228.

[71] M. Kulmala, M. Maso, J. Mäkelä, L. Pirjola, M. Väkevä, P. Aalto, P. Miikkulainen, K. Hämeri, C. O'dowd, On the formation, growth and composition of nucleation mode particles, Tellus B 53 (2001) 479-490.

List of Table and Figure Captions:

Table 1 A list of instruments commonly for incipient particle measurement.

Table 2 Experimental plan.

Table 3 List of some major positive and negative compounds within the ion spectra measured by the APi-TOF.

Fig. 1. A schematic diagram of the experimental setup.

Fig. 2. PSM and DMA-measured size distributions of blank flame-generated sub-3 nm particles at H_{AB} = 5 mm.

Fig. 3. Effect of sampling height on: (a) PSM-measured size distributions and (b) neutral fractions of blank flame-generated sub-3 nm particles.

Fig. 4. Mass spectrum of blank flame-generated ions measured by the APi-TOF. a) mass spectrum of positive ions; inset plot: mass defect plot of the positive ions (size of the circle indicates the relative abundance of the species); the blue line shows the mass defects of C_nH_n clusters and b) mass spectrum of negative ions.

Fig. 5. PSM and DMA-measured size distributions of flame-generated sub-3 nm particles during the flame synthesis of TiO_2. The sampling probe height was 5 mm and *TTIP* feed rate was 0.170 mmol/hr.

Fig. 6. Mass spectrum of flame-generated sub-3 nm particles measured by the APi-TOF during the synthesis of TiO_2. The identified peaks are shown in gray color: a) shows positively charged particles; inset plot: mass defect plot of the positive ions (size of the circle indicates the relative abundance of the species) and b) shows negatively charged particles; inset plot: mass defect plot of the negative ions (size of the circle indicates the relative abundance of the species); the blue

line shows the mass defect of clusters with NO_3 as the core and TiO_2NO_3 as the additional group.

Fig. 7. Effect of the precursor feed rate and sampling height on: (a) PSM-measured size distributions and (b) neutral fractions of flame-generated sub-3 nm particles. Fig. 7a displays the size distributions of sub-3 nm particles synthesized at a feed rate of 0.213 mmol/hr at H_{AB} = 10 and 20 mm. (a). Fig. 7b shows the neutral fractions of 1.17 nm particles generated with a *TTIP* feed rate of 0.213 mmol/hr at H_{AB} = 10 and 20 mm.

Tables

Table 1 A list of instruments commonly for incipient particle measurement.

Instrument	Acronym	Function
Differential Mobility Analyzer	DMA	Classify particles as a function of mobility size
Tandem Differential Mobility Analyzer	TDMA	Determine particle charge fraction as a function of particle mobility size
Condensation Particle Counter	CPC	Measure particle number concentrations
Butanol CPC	bCPC	Measure particle number concentrations with butanol as the working fluid
Particle Size Magnifier	PSM	Grow particles as small as 1 nm to a detectable size using diethylene glycol as the working fluid
Molecular Beam Mass Spectrometer	MBMS	Detect the chemical composition of ions through the well-designed compact skimmer inlet system
Atmospheric Pressure Interface Time-of-Flight Mass Spectrometer	APi-TOF MS	Detect the composition of ambient ions with a mass accuracy higher than 0.002% and a resolving power of 3000 Th/Th
Charged Particle Remover	CPR	Remove charged ions and particles

Table 2 Experimental plan.

Test #	Probe height (H_{AB}) [mm]	*TTIP* feed rate [mmol/h]
1	5	0
2	10	0
3	15	0
4	20	0
5	5	0.043
6	5	0.085
7	5	0.128
8	5	0.170
9	5	0.213
10	10	0.213
11	20	0.213

Table 3 List of some major positive and negative compounds within the ion spectra measured by the APi-TOF.

Identified positive ions		Identified negative ions	
Integer m/z	**Chemical formula**	**Integer m/z**	**Chemical formula**
97	$HC_4O_3^+$	62	NO_3^-
117	$TiH_5O_4^+$	204	$TiN_2O_8^-$
132	$TiH_4O_5^+$	220	$TiN_2O_9^-$
143	$TiC_2H_7O_4^+$	236	$TiN_2O_{10}^-$
146	$TiCH_6O_5^+$	266	$TiN_3O_{11}^-$
159	$TiC_2H_7O_5^+$	286	$Ti_2NO_{11}^-$
173	$TiC_3H_9O_5^+$	348	$Ti_2N_2O_{14}^-$
187	$TiC_4H_{11}O_5^+$	396	$Ti_3N_2O_{14}^-$
229	$TiC_6H_{13}O_6^+$	460	$Ti_2N_2O_{18}^-$

Figure 1 color on web

Click here to download high resolution image

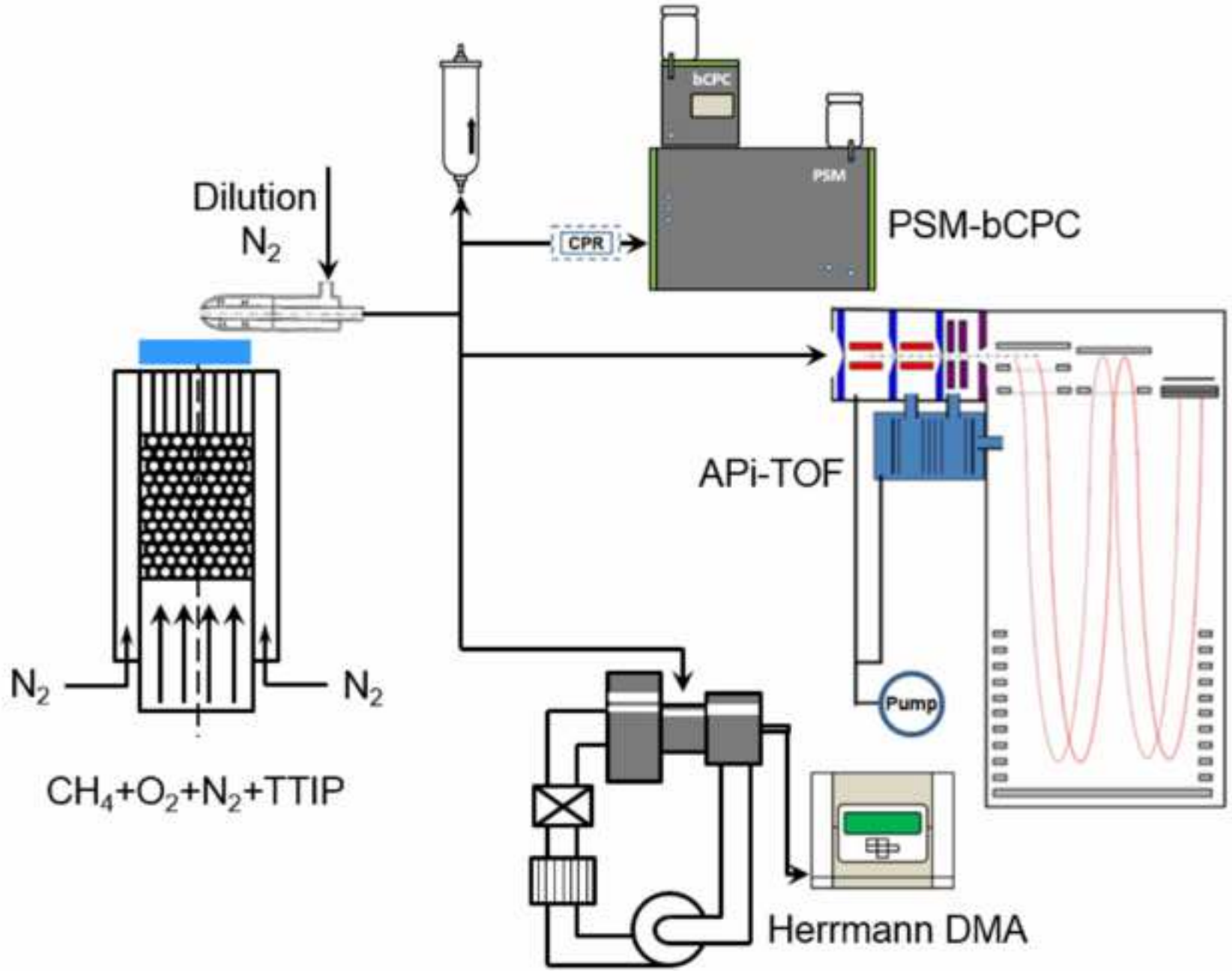

Figure 2 color on web

Click here to download high resolution image

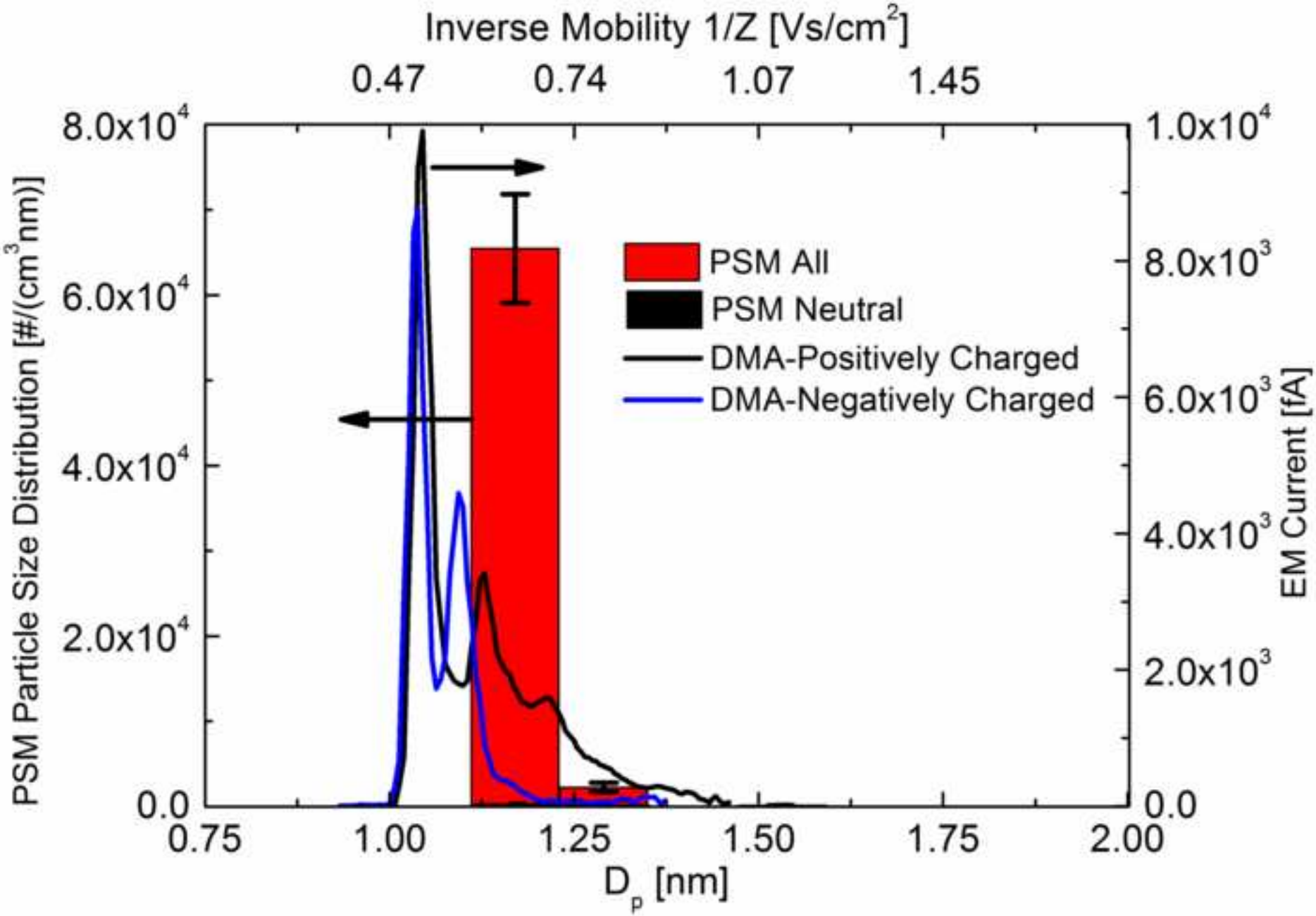

Figure 3 color on web

Click here to download high resolution image

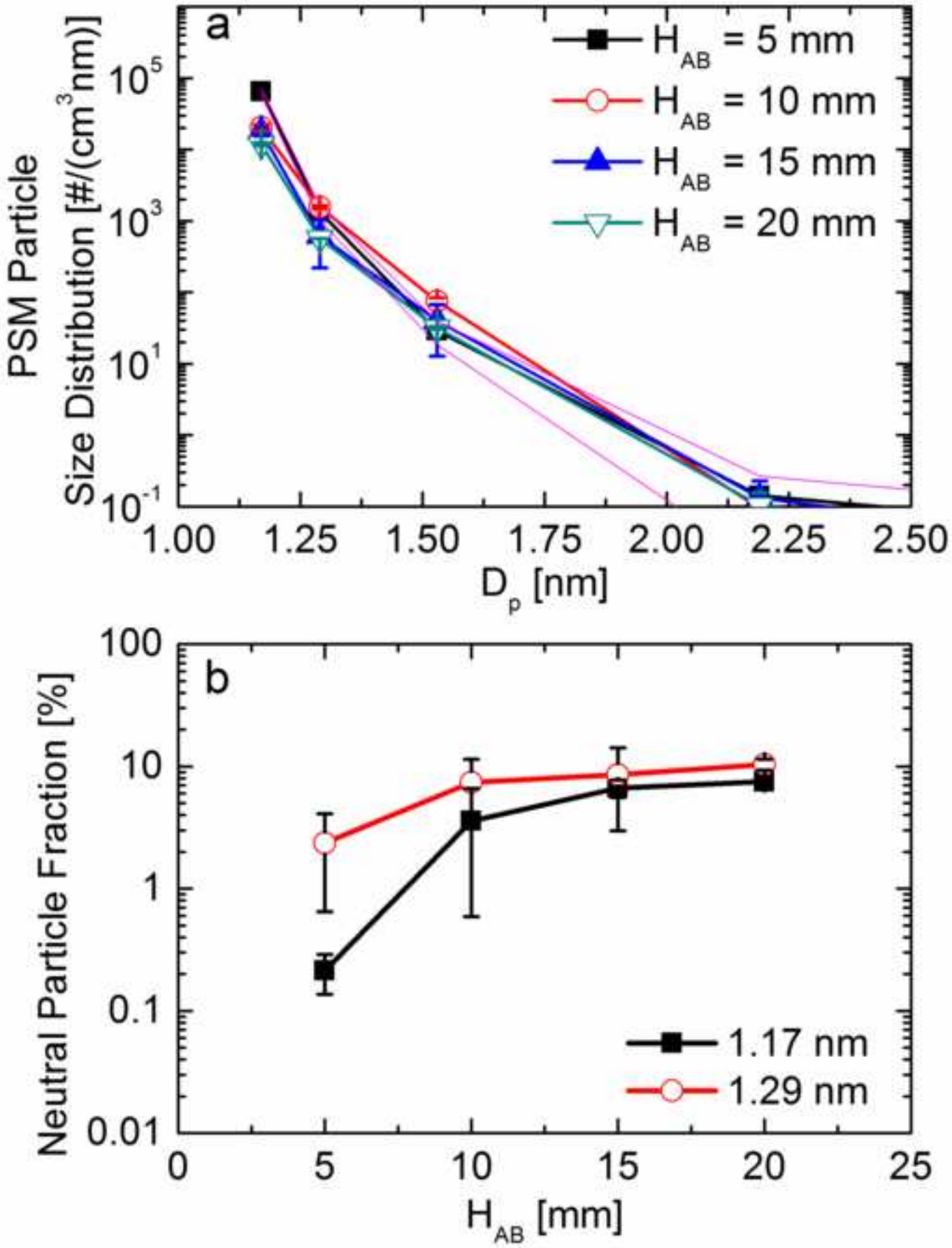

Figure 4 color on web

Click here to download high resolution image

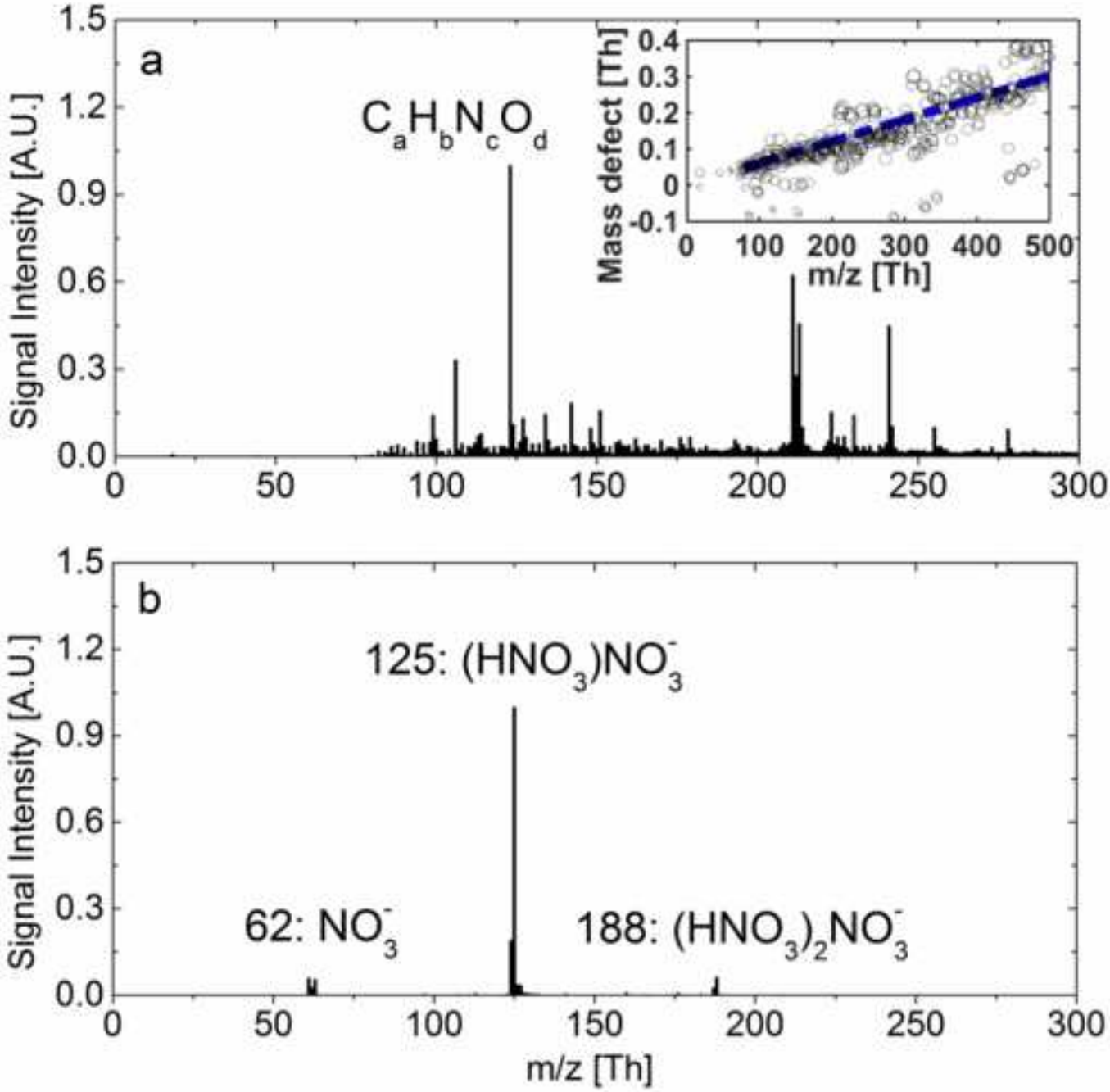

Figure 5 color on web

Click here to download high resolution image

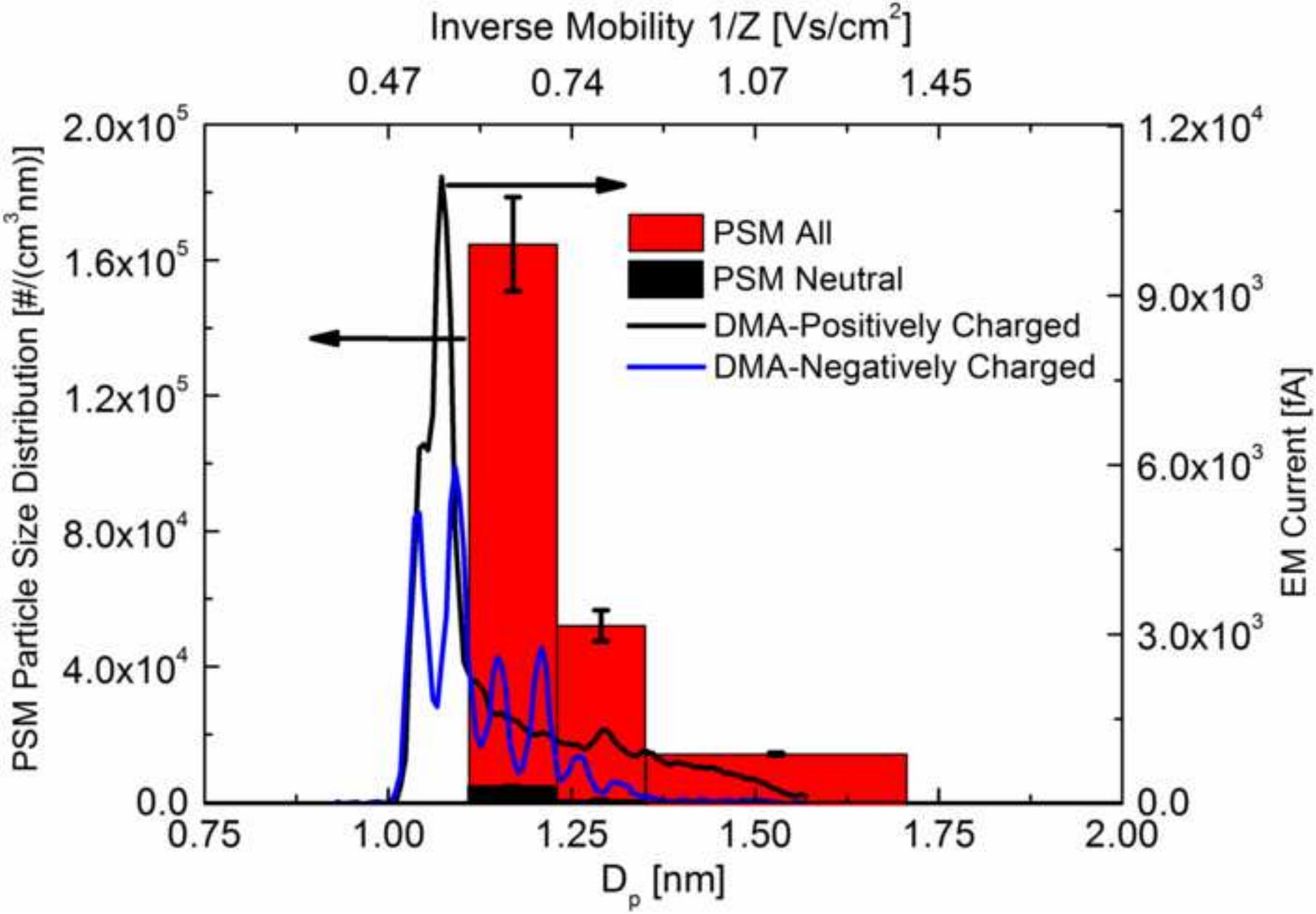

Figure 6 color on web

Click here to download high resolution image

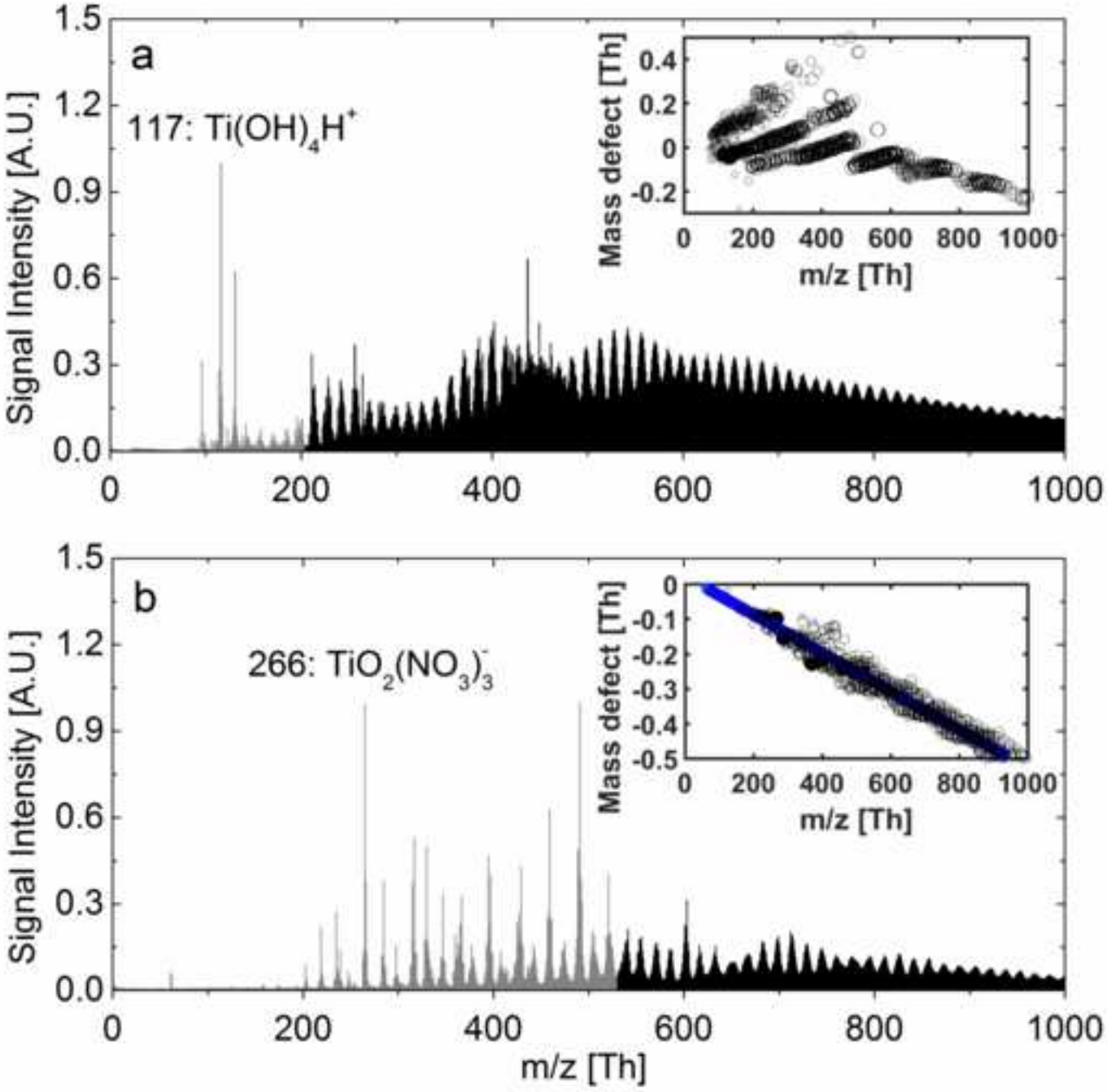

Figure 7 color on web

Click here to download high resolution image

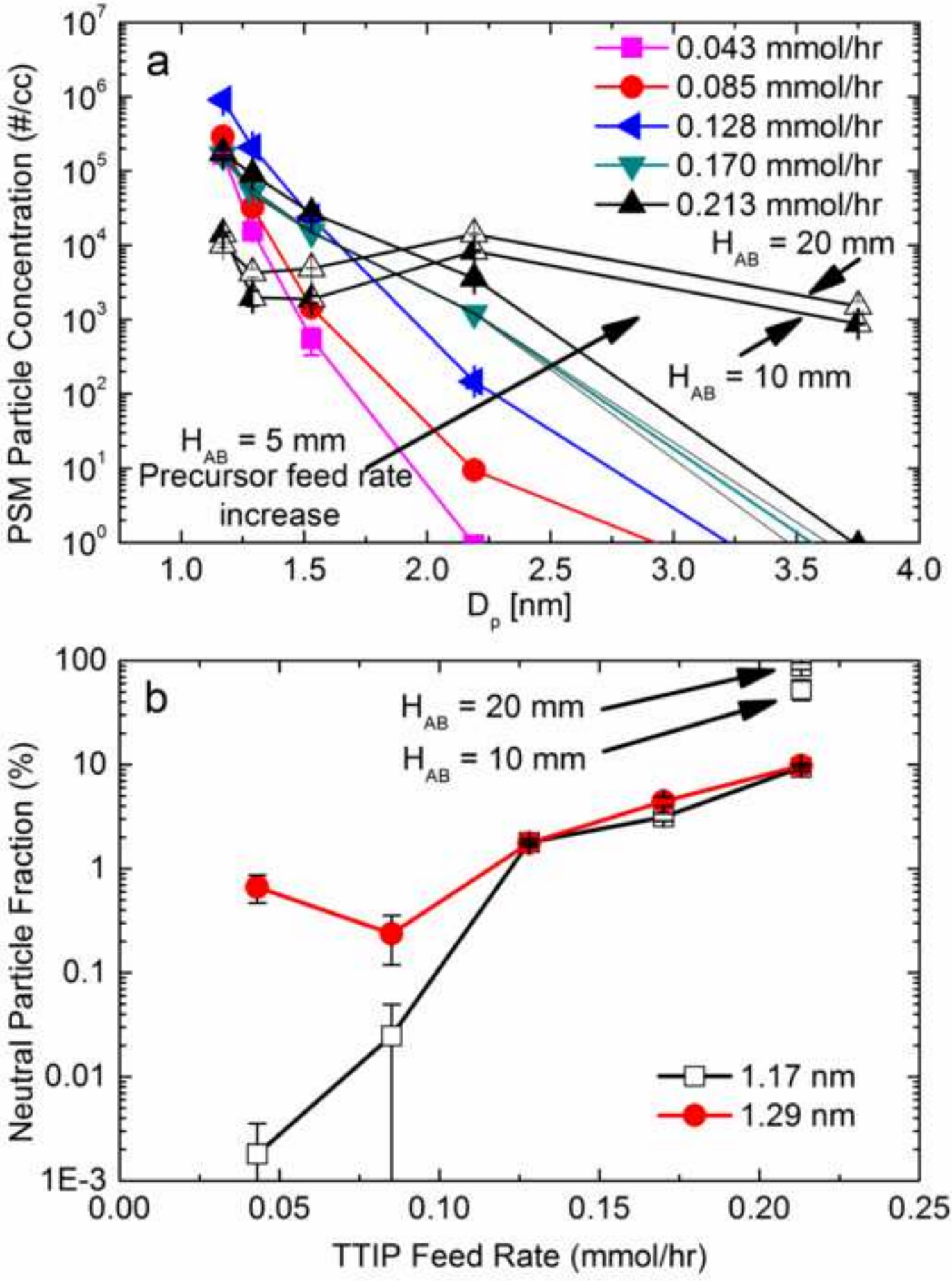

Figure 1 black-and-white in print

Click here to download high resolution image

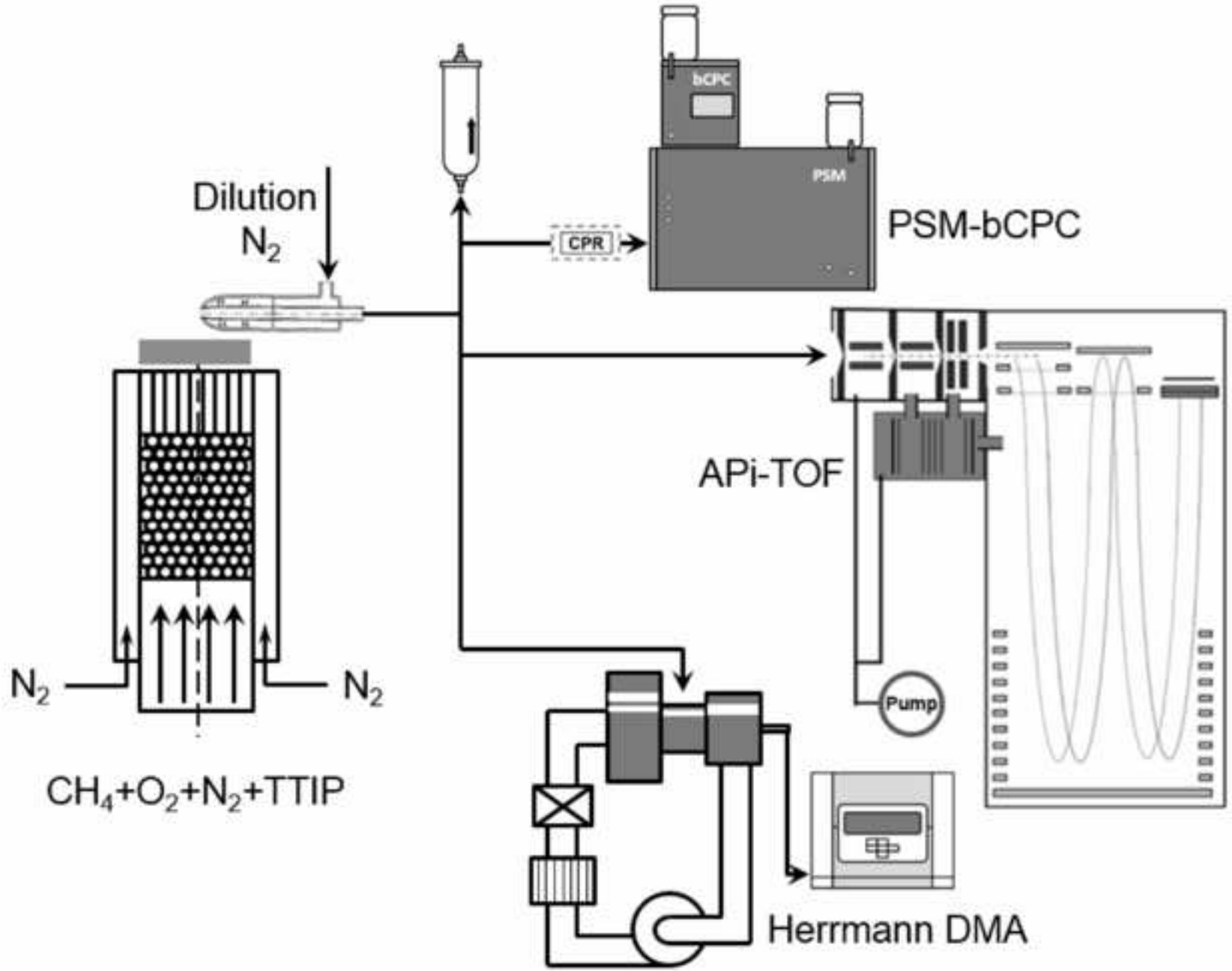

Figure 2 black-and-white in print

Click here to download high resolution image

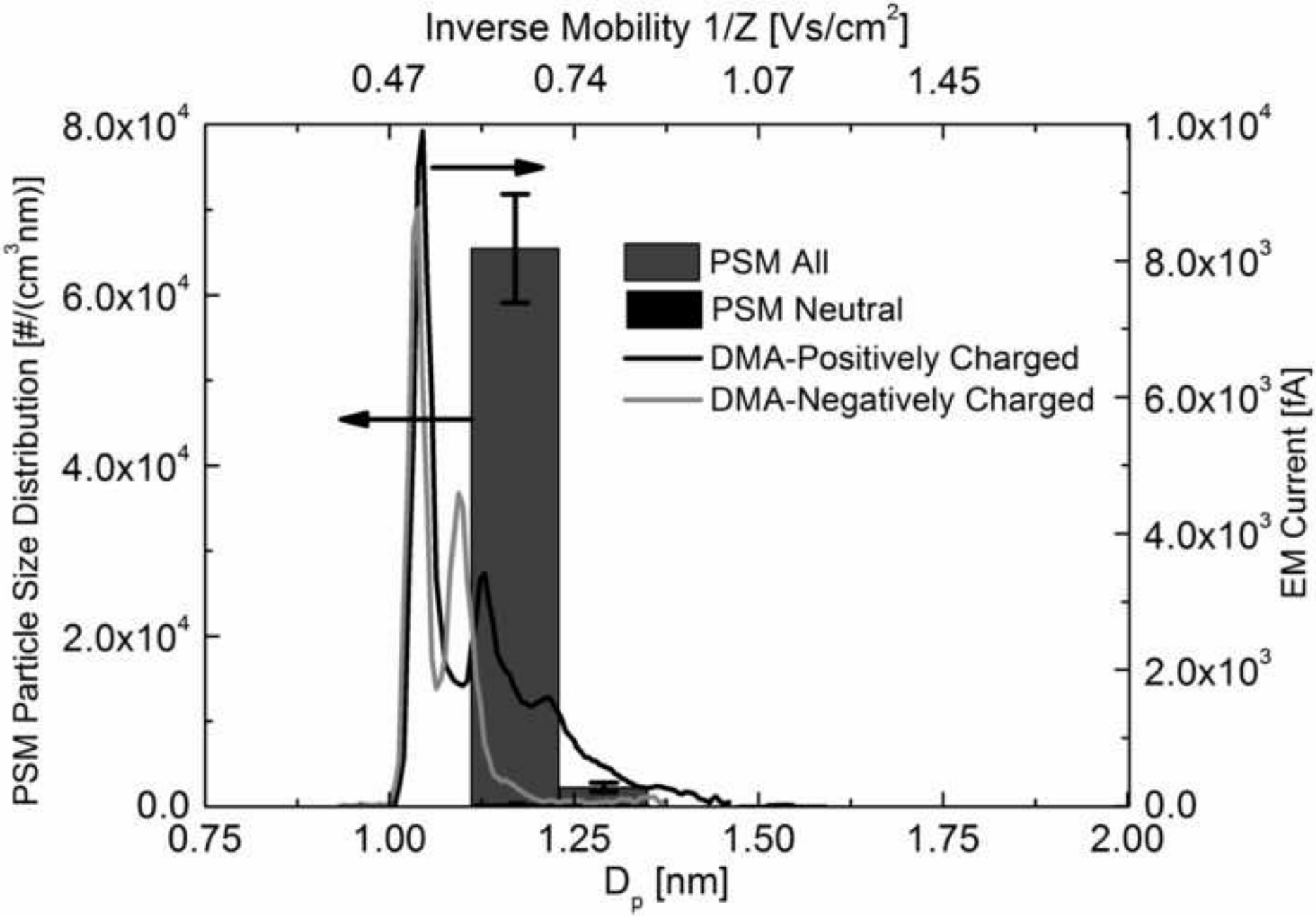

Figure 3 black-and-white in print
Click here to download high resolution image

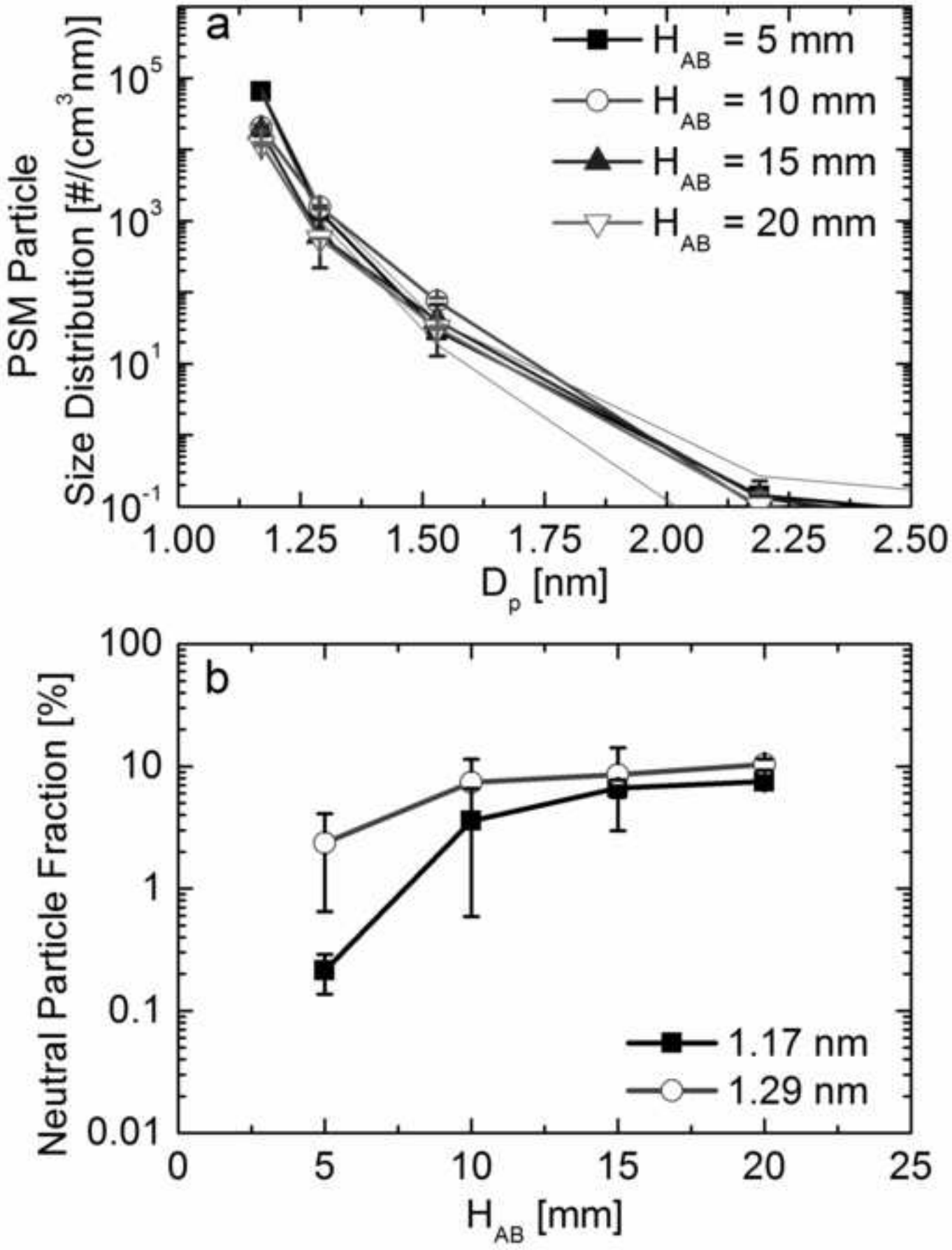

Figure 4 black-and-white in print

Click here to download high resolution image

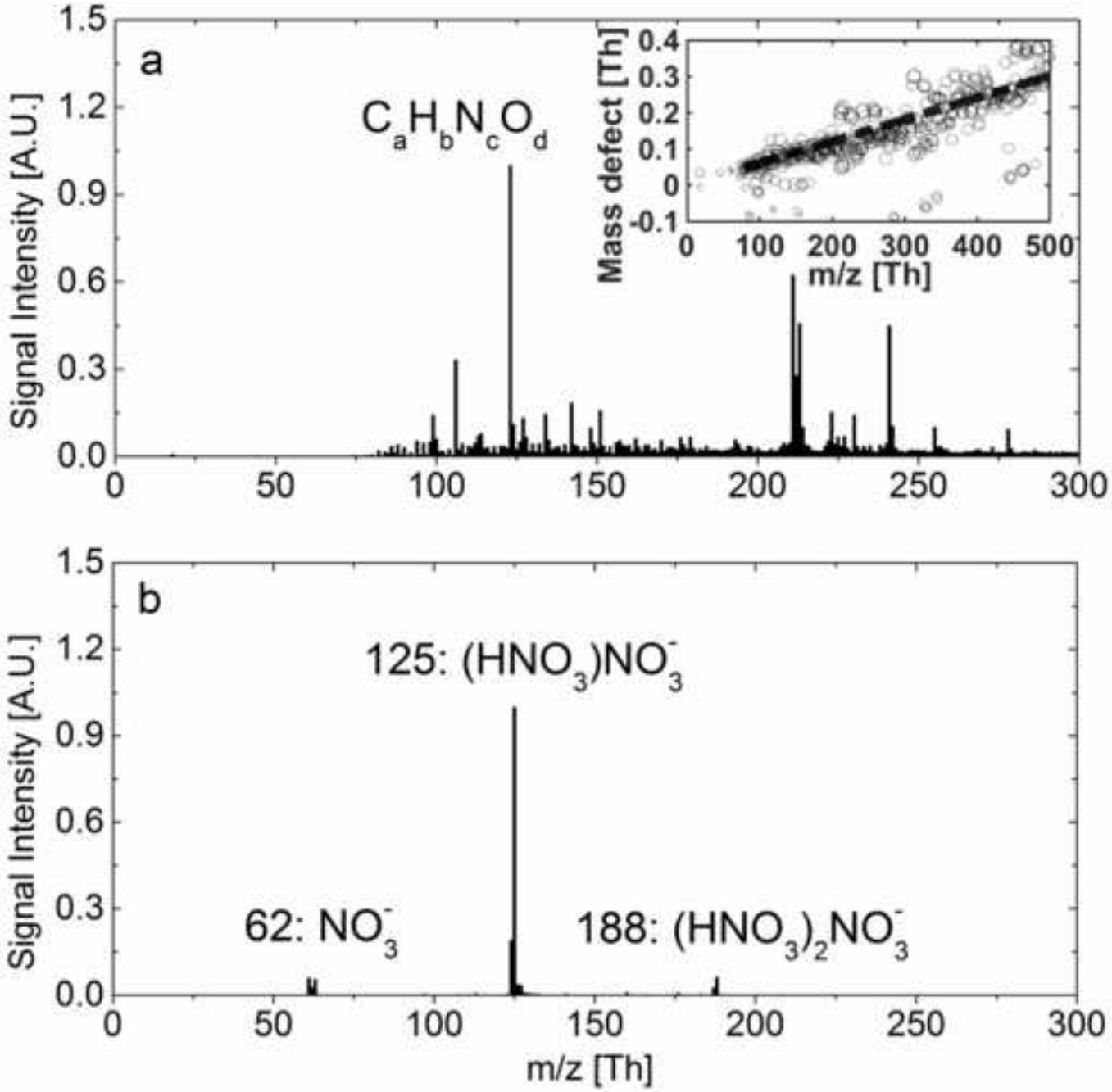

Figure 5 black-and-white in print
Click here to download high resolution image

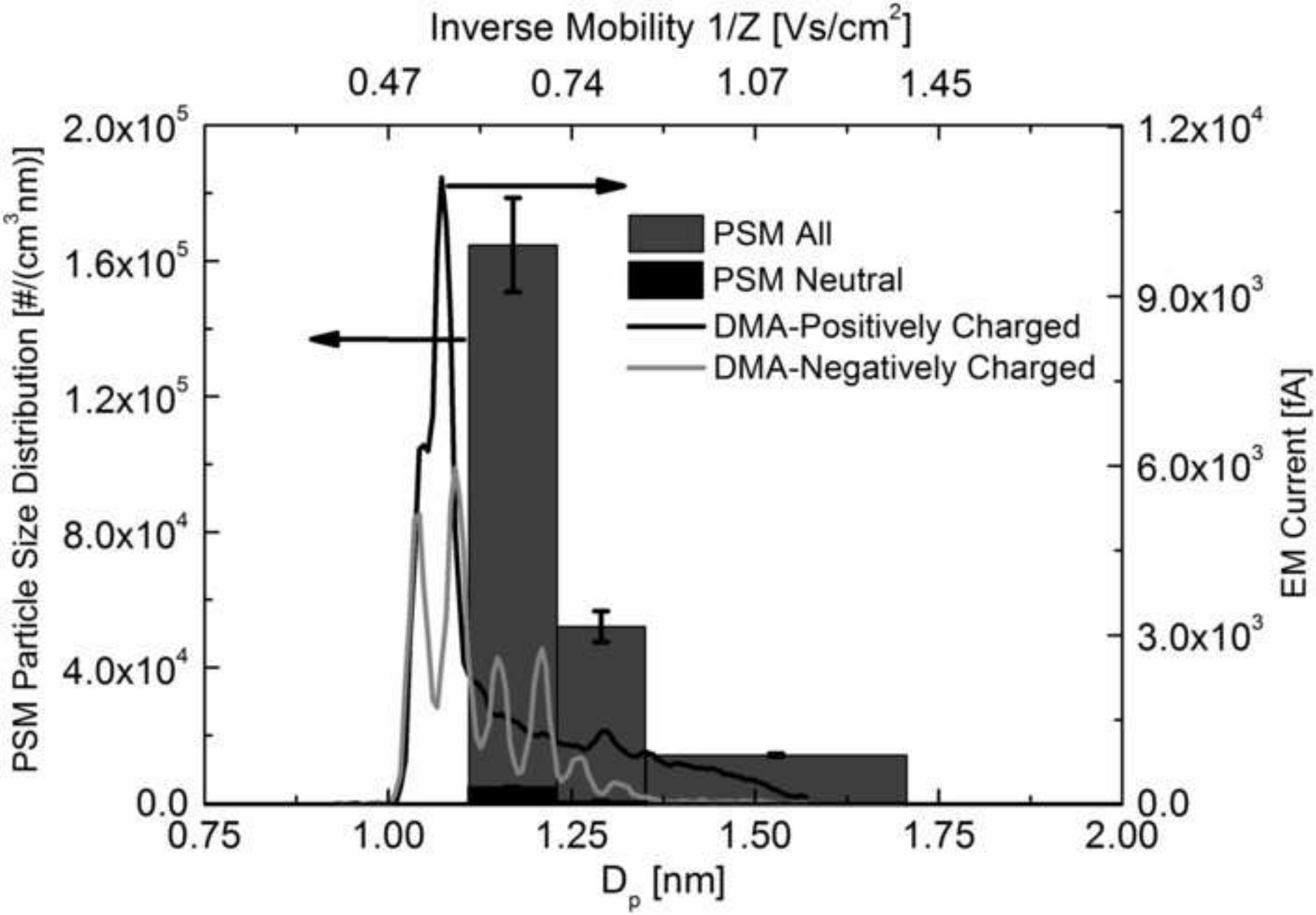

Figure 6 black-and-white in print

Click here to download high resolution image

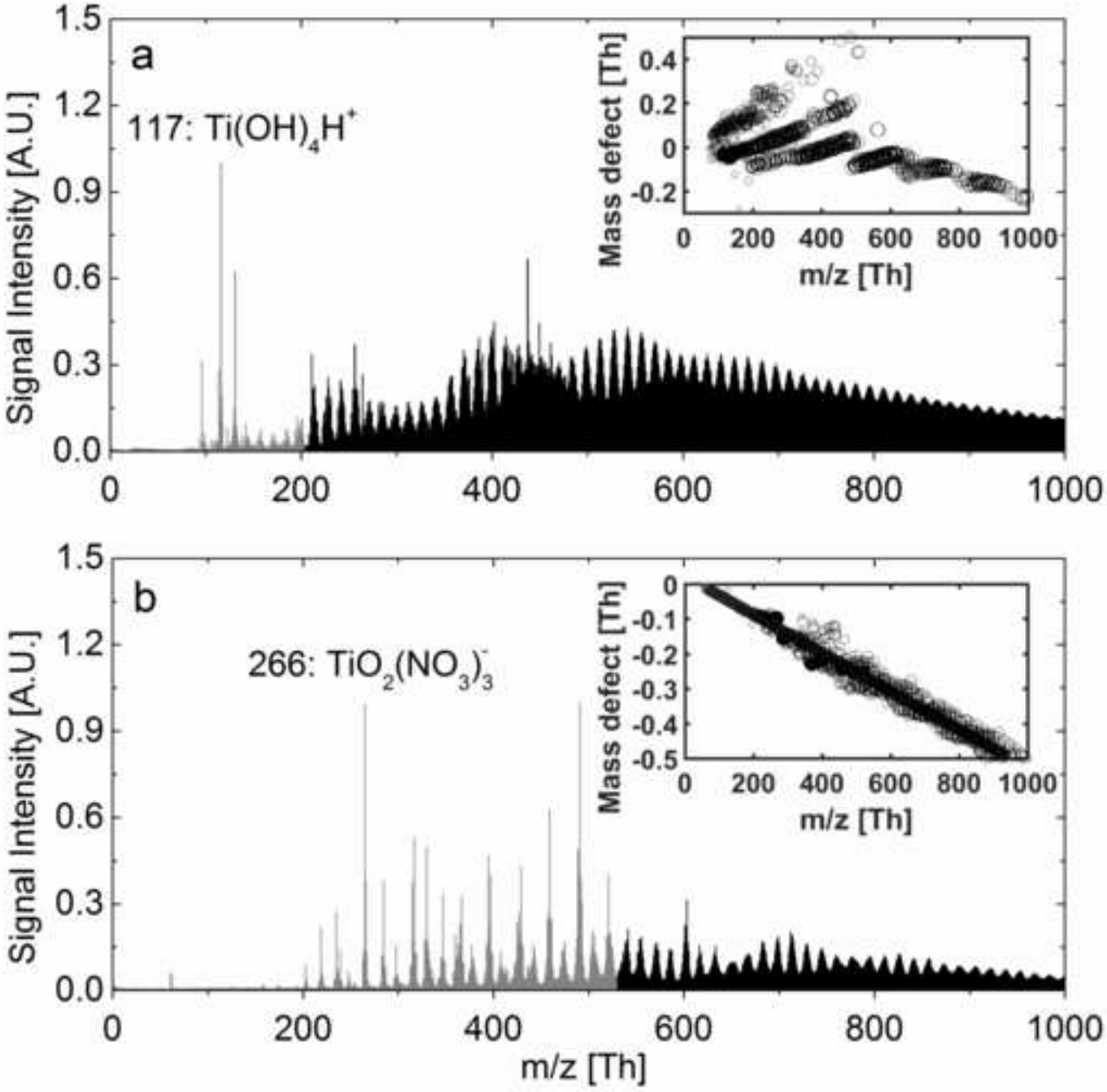

Figure 7 black-and-white in print

Click here to download high resolution image

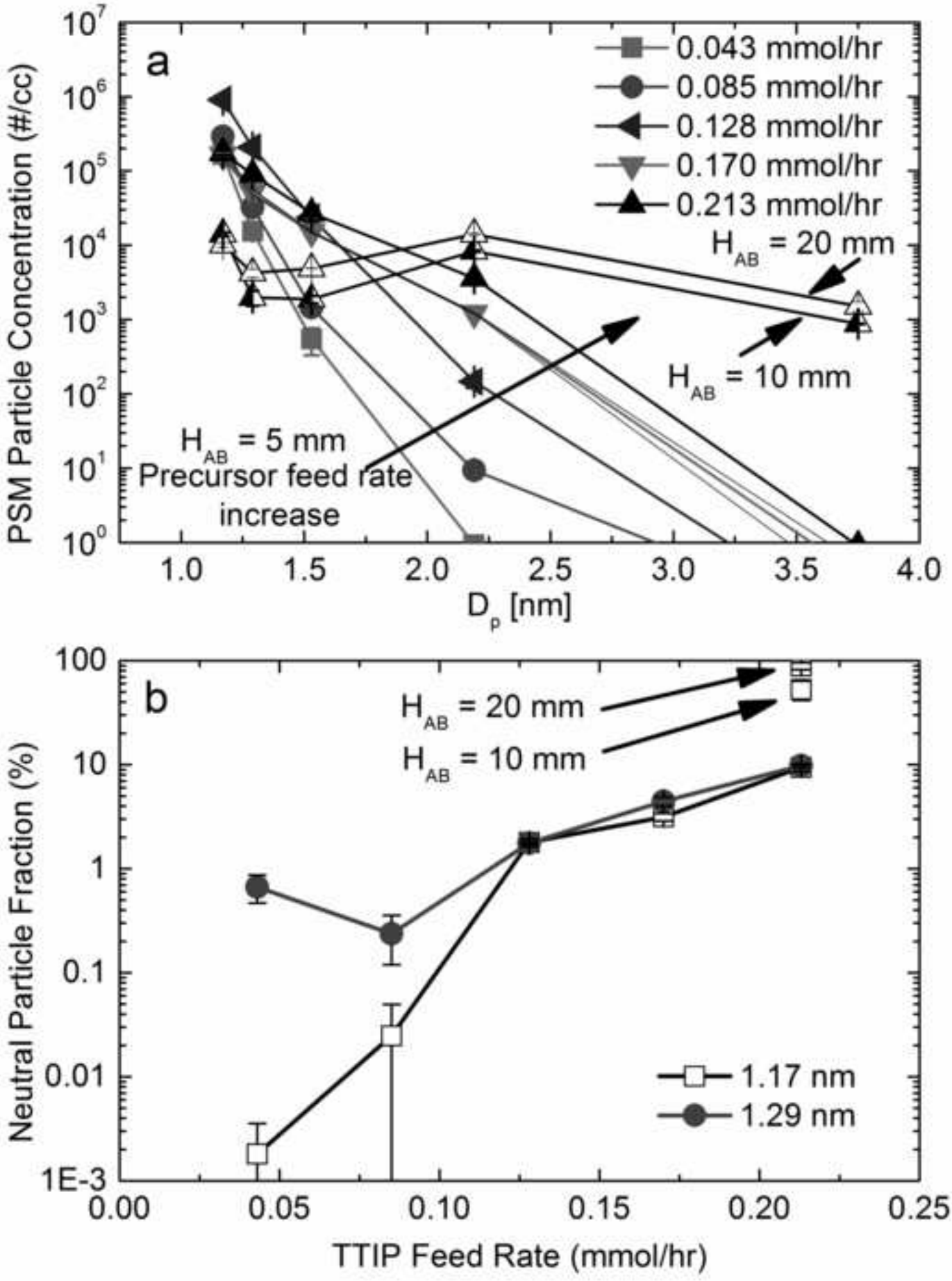

Supplementary Material

Click here to download Supplementary Material: SupplementaryContent_Wang_CNF.docx